crystals

MDPI

Review

TWIP Steels at a Crossroads: Two Decades of Research, Persistent Gaps, and Strategies for Advancing Their Potential

Samjukta Sinha [1], Abhishek Ghosh [2,*], Prabhat Das [3], Amitava Basu Mallick [1] and Manojit Ghosh [1,4]

[1] Department of Metallurgy and Materials Engineering, Indian Institute of Engineering Science and Technology, Shibpur, Howrah 711103, West Bengal, India; samjukta.sinha@gmail.com (S.S.); abasumallick@metal.iiests.ac.in (A.B.M.); mghosh@metal.iiests.ac.in (M.G.)
[2] Department of Mechanical Engineering, Thapar Institute of Engineering and Technology, Patiala 147004, Punjab, India
[3] Department of Computer Science and Engineering, Centre of Excellence in Artificial Intelligence, Adamas University, Barasat 700126, West Bengal, India; prabhat1.das@adamasuniversity.ac.in
[4] Chirasree Centre for Sustainable Infrastructure Development, Indian Institute of Engineering Science and Technology, Shibpur, Howrah 711103, West Bengal, India
* Correspondence: abhishek.me.08@gmail.com

Abstract

Twinning-induced plasticity (TWIP) steels have attracted considerable attention over the past two decades owing to their exceptional combination of strength, ductility, and strain-hardening capability. Despite extensive investigations into their alloy chemistry, stacking-fault energy, deformation mechanisms, microstructural evolution, and thermomechanical processing, the overall development of TWIP-steel research and its transition toward broader practical utilization remain incompletely assessed. This work presents a combined bibliometric and critical review of TWIP-steel research from 2005 to 17 September 2026. A bibliometric analysis of 1312 records retrieved from Scopus was conducted to examine publication trends, international research collaborations, influential publications, and the evolution of seven major research themes across three distinct phases. The findings of this analysis provide a basis for reviewing the major scientific developments during these periods, thereby establishing a connection between the bibliometric results and the critical review of the existing literature. Particular emphasis is placed on the evolution of the field, the recent moderation in research activity, and the emerging role of data-driven approaches, especially machine learning, in TWIP-steel development. The study further identifies the principal unresolved research gaps and outlines future directions toward more integrated, predictive, and application-oriented development of TWIP steels.

Keywords: TWIP steel; stacking fault energy; deformation twins; thermomechanical processing; bibliometric analysis; machine learning

Check for updates

Academic Editor: Binbin Wu

Received: 28 September 2026
Revised: 30 October 2026
Accepted: 11 November 2026
Published: 16 November 2026

Copyright: © 2026 by the authors. Licensee MDPI, Basel, Switzerland. This article is an open access article distributed under the terms and conditions of the Creative Commons Attribution (CC BY) license.

1. Introduction

In the era of modern automotive development, the focus lies on developing vehicles that maintain passenger safety and lower CO_2 emissions. To achieve these goals, manufacturers are adopting advanced materials like twinning-induced plasticity (TWIP) steels, known for their remarkable combination of tensile strength and ductility, as evident from Figure 1. This advanced high-strength steel (AHSS) is ideal for designing cars that are in demand to withstand extreme forces under critical situations while remaining lightweight [1,2]. Figure 2 shows the use of different steels in a vehicle body [3]. TWIP steel is primarily composed of C and Mn with alloying elements such as Al and Si [4]. Mn content between

15 wt.% and 30 wt.% tends to stabilize the austenite at room temperature (RT), resulting in a single-phase FCC structure [1,5]. The exceptional tensile strength beyond 1000 MPa and total elongation exceeding 50% can be attributed to the presence of twins [6]. Deformation twinning in TWIP steels is generally favoured at stacking fault energies (SFEs) of approximately 20–40 mJ/m^2. These steels typically contain 15–30 wt.% Mn, with Al and Si additions commonly ranging from 0 to 3 wt.% each, depending on the alloy composition and the desired deformation behaviour [7]. Higher Mn content prevents undesirable transformation from γ (austenite) to ε (martensite), which imparts brittleness [8,9]. Al addition plays a vital role in controlling the SFE and suppresses the martensite transformation. It also prevents the formation of carbide Fe_3C and helps with a slight reduction in density. Al addition also enhances the resistance of TWIP steels against hydrogen embrittlement [1]. Addition of Si decreases the SFE and also resists carbide precipitation [7]. With an appropriate combination of alloying elements Al and Si, the SFE can be adjusted between 15–40 mJ/m^2, where the TWIP effect can be restored [10]. Maintaining an upper bound of C of 0.3 wt.% is necessary for stabilizing austenite, which otherwise may result in carbide precipitation and impair ductility [11]. Additionally, Cr and Ce are frequently introduced as alloying elements in TWIP steel to enhance its mechanical properties. Adding Cr up to 15 wt.% results in improved tensile and yield strength in TWIP steels, attributed through solid solution strengthening [12]. In a study conducted by Lingqiang Zhong et al. [13], the effects of Ce addition to the matrix composition of TWIP steel were investigated. The findings revealed that the addition of 0.15 wt.% Ce demonstrated optimal ultimate tensile strength (UTS) and elongation, reaching values of 1023 MPa and 92%, respectively.

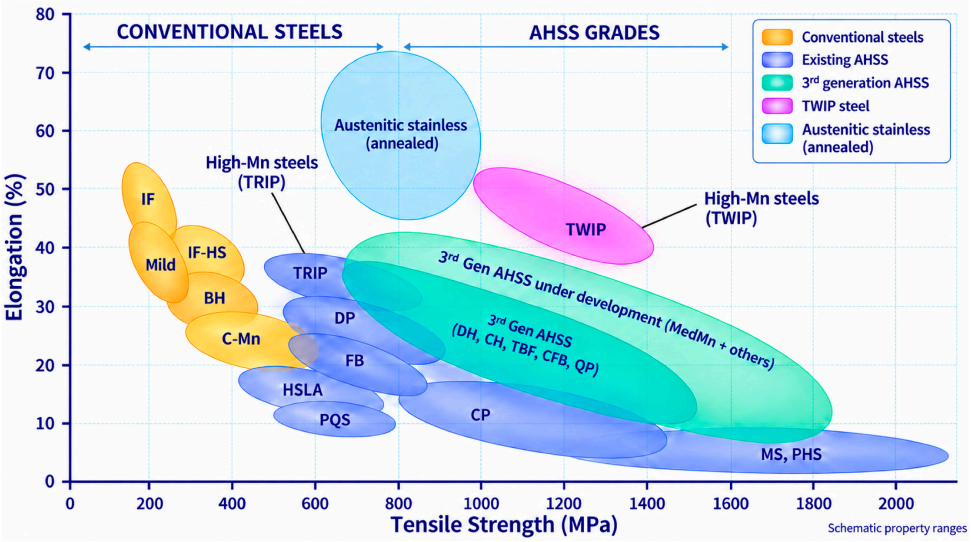


Figure 1. Strength ductility diagram of different AHSS and conventional steels [14].

Strain hardening is the primary strengthening mechanism in TWIP steels, where mechanical twins that form during straining decrease the effective mean free path of dislocations. This reduction leads to an increase in flow stress, a phenomenon also referred to as the dynamic Hall–Petch effect [1]. Several researchers have investigated the mechanical properties of TWIP steel at different strain rates and temperature correlating twin density and size. As the strain rate increases, the thickness of the deformation twins decreases. This leads to an increase in both tensile and yield strength because a higher stress is needed for dislocations to traverse the twin boundaries [15]. In the FCC austenitic matrix, deformation twinning occurs through the coordinated glide of Shockley partial dislocations with Burgers vectors of $\frac{a}{6}\langle 112\rangle$ on successive (111) planes, where 'a' is the lattice parameter. A perfect dislocation

can dissociate into two Shockley partials: $\frac{a}{2}[1\bar{1}0] \rightarrow \frac{a}{6}[2\bar{1}\bar{1}] + \frac{a}{6}[1\bar{2}1]$. The leading partial creates a stacking fault, whereas passage of the trailing partial on the same plane restores the FCC stacking sequence. When twinning partials instead glide on successive adjacent planes, their accumulated shear produces a deformation twin. Continued partial-dislocation glide enables twin growth, while the newly formed twin boundaries restrict dislocation motion and promote dislocation accumulation, sustaining strain hardening [16].

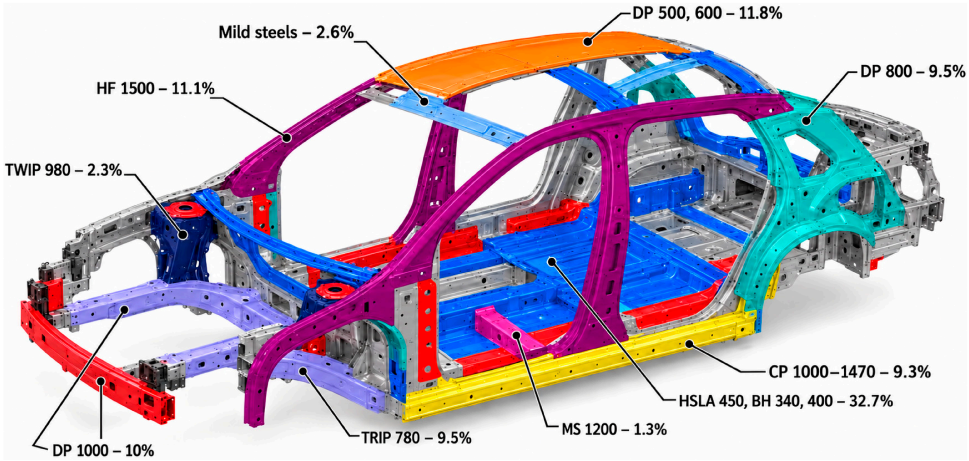


Figure 2. Application of different steels in a vehicle body [3].

Analyzing past research is essential for understanding the present status, evolution, and emerging priorities of a scientific field. Although TWIP steels have been extensively investigated over the past two decades, relatively few studies have systematically examined how research activity in this area has evolved at the global level. To the best of the authors' knowledge, a comprehensive bibliometric assessment specifically focused on TWIP steels remains limited. Bibliometric analysis provides an effective means of quantitatively mapping the development of a research domain by identifying publication trends, influential contributions, collaborative networks, and emerging thematic directions [17].

Bibliometric analysis employs mathematical and statistical approaches to examine the scientific literature and associated information networks. It enables the identification of research collaborations, citation and co-citation relationships, dominant research themes, knowledge clusters, and shifts in scientific focus over time [18]. Such approaches have been widely applied in diverse fields, including COVID-19 vaccination [19], the hydrogen economy [20], computational intelligence [21], microbial cells [22], and social cohesion [23]. However, TWIP-steel research still lacks an integrated assessment that combines bibliometric mapping with a critical evaluation of the metallurgical advances achieved since the emergence of this advanced high-strength steel.

Accordingly, the present study provides a combined bibliometric and critical review of nearly two decades of TWIP-steel research from 2005 to 17 September 2026. Bibliometric visualization using VOSviewer (version 1.6.19, developed by the Centre for Science and Technology Studies (CWTS), Leiden University, Leiden, The Netherlands) is employed to examine the evolution of publication output, leading countries, and highly cited contributions. In parallel, the major scientific developments in TWIP steels are critically reviewed, including alloy chemistry, stacking-fault energy, deformation mechanisms, thermomechanical processing, microstructural evolution, mechanical behaviour, hydrogen embrittlement, fatigue, and emerging machine-learning applications. Beyond summarizing past progress, the study identifies the principal technological and methodological gaps that continue to restrict wider implementation of TWIP steels and outlines future research directions aimed at advancing alloy design, processing, data-driven modelling, and engineering applica-

bility. The research phases identified from the publication trends and the major research themes presented in Section 3.4 provides the basis for organising the following critical review. This approach provides a systematic basis for examining the major scientific developments in relation to the research trends and thematic patterns identified through the bibliometric analysis.

The remainder of this review is organised as follows. Section 2 presents the research methodology, including the data source and search strategy (Section 2.1), bibliometric mapping methods (Section 2.2), and the approach used to integrate the bibliometric findings with the critical literature review (Section 2.3). Section 3 presents the results of the bibliometric analysis, covering annual publication trends and the identification of research phases (Section 3.1), country-wise publication output, international collaborations, and citation impact (Section 3.2), highly cited publications (Section 3.3), and the evolution of major research themes across the three phases (Section 3.4). Based on these findings, Section 4 critically reviews the major scientific developments in TWIP steels, focusing on stacking fault energy and deformation mechanisms (Section 4.1), thermomechanical processing, microstructural evolution, and alloy design (Section 4.2), followed by hydrogen embrittlement (Section 4.3), fatigue behaviour and fracture mechanisms in (Section 4.4) which has shown an increase in its share of publications among service-related research themes. Section 5 discusses the applications of machine learning (ML) in TWIP-steel research, an emerging area with relatively limited publications. Section 6 discusses the scientific trends and research perspectives emerging from the bibliometric analysis. Section 7 identifies existing research gaps and outlines potential directions for future investigations, while Section 8 presents the concluding remarks.

2. Materials and Methods

2.1. Data Source and Search Strategy

All bibliometric data were extracted from the Scopus database using a query string. The query was applied to the title, abstract and keyword fields:

TITLE-ABS-KEY (“TWIP steel” OR “twinning induced plasticity steel” OR “TRIP/TWIP steel”) AND PUBYEAR > 2004 AND PUBYEAR < 2027.

The search covered publications from 2005 to 2026 and yielded a total of 1312 records as of 17 September 2026. All returned document types and languages were retained because the purpose was to map the indexed research domain. The first publication in the Scopus database collection dates back to 2005. Seven different types of documents were identified. Table 1 displays the document types, quantities, and corresponding percentages. “Article” was the most common document type, accounting for 81.93% of the publications. The second and third most popular document types were “conference paper” and “review article”, respectively. Finally, the following document types appeared less frequently in the database: “book chapter,” “letter,” “erratum,” and “short survey.” English, Japanese, Chinese, Korean, French, Italian, Turkish, Russian, and German were among the languages used for publication, with English accounting for 89.31% of the total.

Table 1. Distribution of document types in the TWIP-steel Scopus database.

Rank	Document Type	Quantity	Percentage
1	Article	1075	81.93%
2	Conference Paper	191	14.55%
3	Review	26	1.98%
4	Book Chapter	14	1.06%

Table 1. *Cont.*

Rank	Document Type	Quantity	Percentage
5	Letter	3	0.23%
6	Erratum	2	0.15%
7	Short Survey	1	0.07%

2.2. Bibliometric Mapping Methodology

The 1312 records retrieved from Scopus were exported in CSV format, including their complete bibliographic information, and subsequently subjected to three complementary analyses: (i) descriptive analysis, encompassing the annual publication output and the distribution of document types and languages, derived directly from the bibliographic records (Table 1, Figure 3); (ii) country-level co-authorship analysis, conducted to examine international research collaborations and their network structure (Figure 4); and (iii) citation analysis, performed at both the country level (Table 2, Figure 5) and the individual document level (Section 3.3) to assess research impact and citation patterns. The country-level network maps were generated using VOSviewer software, which employs the Visualisation of Similarities (VOS) mapping framework developed by van Eck and Waltman [18]. The VOS method represents relationships between objects in a low-dimensional space, where the distance between objects reflects their degree of similarity, with more closely related objects positioned nearer to each other [18]. The following section describes the underlying data processing procedures and mapping methods:

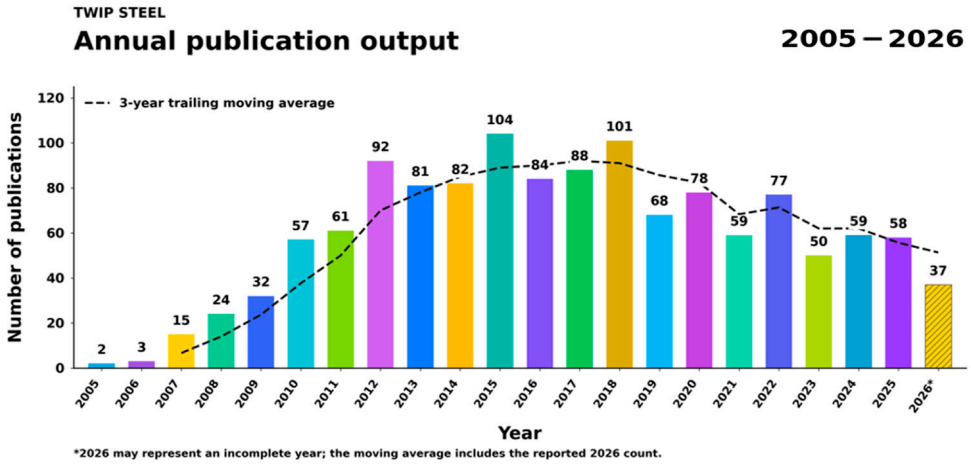


Figure 3. Annual publications in the database-delimited TWIP-steel corpus, 2005–17 September 2026.

Country network: Each country or territory identified from the authors' affiliations was represented as a node (i) in the co-authorship network. The full counting method has been adopted, whereby each publication was assigned to all countries represented in its authors' affiliations. Accordingly, a publication involving authors from multiple countries contributed one publication count to each participating country. The weight of each node (i) represents the total number of publications associated with that country, while the link weight (c_{ij}) between two countries (i and j) indicates the number of publications jointly authored by researchers from those countries. A minimum threshold of one publication per country was applied, resulting in the inclusion of all 48 countries identified in the dataset (Table 2). For the country-level citation analysis, the total citations received by publications associated with each country were calculated by summing their individual citation counts (Table 2). Similarly, the document-level citation analysis was performed using the citation counts of individual publications obtained directly from Scopus (Section 3.3).

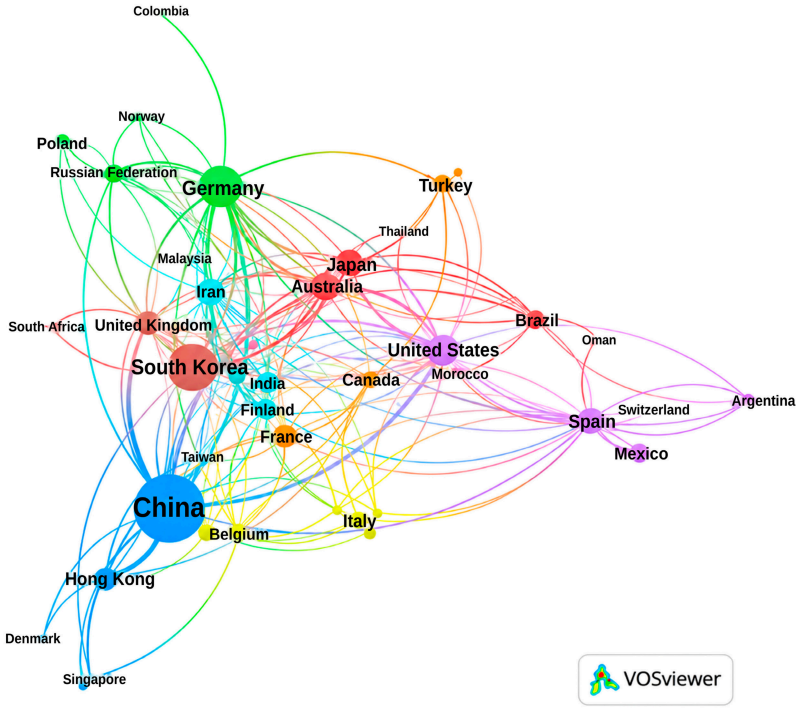


Figure 4. Country co-authorship network for the 2005–2026 TWIP-steel corpus.

Table 2. The prolific countries in TWIP alloy publications, (2005–17 September 2026).

Rank	Country	Documents	Citations
1	China	492	11,278
2	South Korea	222	12,380
3	Germany	180	9570
4	United States	82	5137
5	Australia	74	3707
6	Japan	62	2891
7	Iran	61	2449
8	United Kingdom	58	2340
9	Spain	57	2336
10	France	44	4998
11	Hong Kong	44	2579
12	Finland	39	2060
13	India	38	1934
14	Mexico	37	620
15	Russian Federation	31	2325
16	Turkey	31	651
17	Belgium	27	2071
18	Brazil	22	423
19	Canada	20	821
20	Egypt	20	612
21	Netherlands	20	1443
22	Italy	19	577
23	Poland	18	257
24	Czech Republic	10	14
25	Austria	9	180
26	Argentina	8	52

Table 2. *Cont.*

Rank	Country	Documents	Citations
27	Chile	8	44
28	Sweden	8	340
29	Hungary	7	112
30	Portugal	7	220
31	Taiwan	7	233
32	Norway	6	177
33	Malaysia	5	26
34	Singapore	4	68
35	South Africa	4	160
36	Morocco	3	36
37	United Arab Emirates	3	81
38	Denmark	2	20
39	Israel	2	5
40	Oman	2	29
41	Switzerland	2	153
42	Thailand	2	33
43	Slovenia	2	0
44	Ukraine	2	0
45	Colombia	1	2
46	Macao	1	7
47	Nigeria	1	17
48	Serbia	1	29

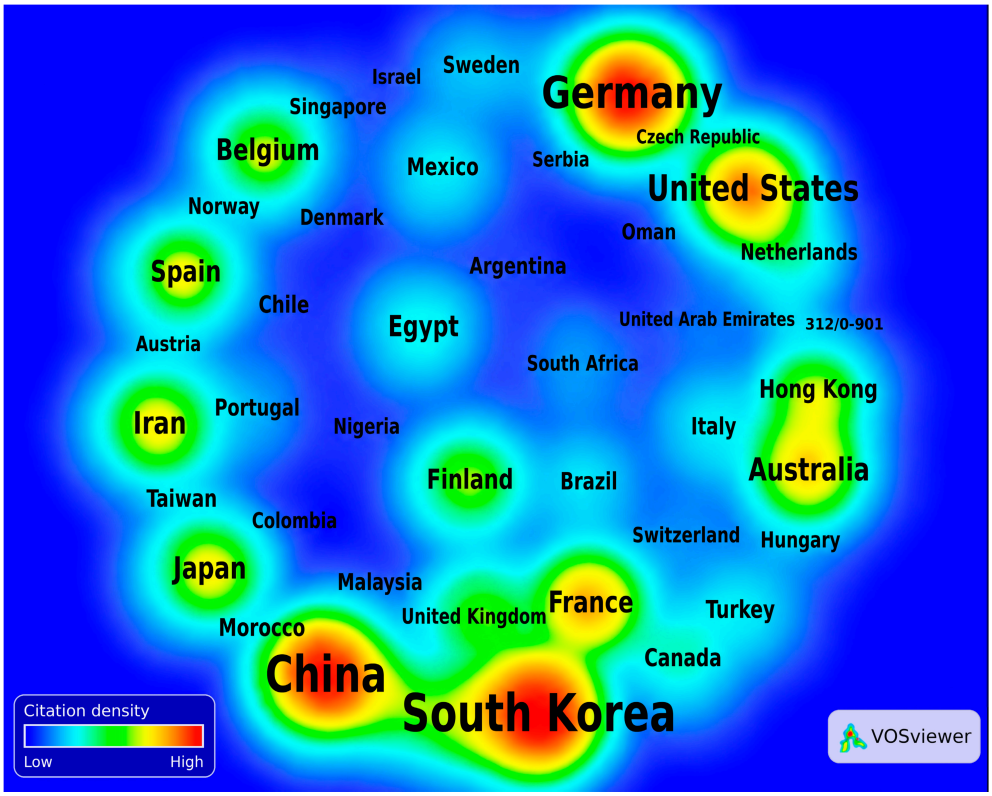


Figure 5. Network density map of countries corresponding to highly cited documents.

Normalisation, mapping and clustering: Since the number of co-authored publications is influenced by the overall publication output of individual countries, the co-authorship link weights were normalised using the association strength method, expressed as

$s_{ij} = c_{ij}/(w_i w_j)$, where c_{ij} represents the number of jointly authored publications between countries i and j, and w_i and w_j represent their respective total link strengths [18]. The two-dimensional position (x_i) of each country was determined by minimising the weighted sum of squared distances, expressed as $V = \sum_{i<j} s_{ij} \left\| x_i - x_j \right\|^2$, while maintaining an average distance of one between all country pairs. This approach ensures that the distances between countries in the map reflect their relative collaboration strengths rather than their total publication output.

Countries with similar collaboration patterns were grouped into clusters by maximising the weighted modularity function, $Q = \sum_{i<j} \delta\left(p_i, p_j\right)\left(s_{ij} - \gamma\right)$, where p_i and p_j indicate the clusters assigned to countries i and j, respectively. The function δ equals one when both countries belong to the same cluster and zero otherwise, while the resolution parameter (γ) was set to 1. In Figure 4, different colours represent the identified collaboration clusters, node sizes indicate the number of publications associated with each country, and link thickness represents the number of jointly authored publications between countries. The citation density map (Figure 5) was generated using Gaussian kernel-based density estimation, in which the citation counts of individual countries were used as weights at their respective positions on the map. The resulting colour gradient, ranging from blue to yellow and then to red, represents increasing citation density, with yellow and red regions indicating higher concentrations of citations and blue regions indicating lower concentrations.

2.3. Integration of the Bibliometric Analysis with the Critical Review

The bibliometric data were further used to organise the critical literature review through three main steps. First, the annual publication trends (Figure 3) were analysed to classify the study period into three distinct research phases. The phases were identified based on changes in annual publication output. From 2012 onwards, the number of publications exceeded 80 records annually, whereas from 2019 onwards, the annual publication count remained below 80 for each complete year. Second, the publications were classified into seven major research themes based on the terms identified in their titles, abstracts, and author keywords. These themes included (A) stacking fault energy, deformation twinning, and strain hardening; (B) thermomechanical processing and microstructure; (C) alloy chemistry and alloy design; (D) hydrogen embrittlement; (E) fatigue, and fracture; (F) ML and data-driven design; and (G) physics-based computational modelling. Since individual publications could address multiple research topics, a single record was allowed to belong to more than one theme. Accordingly, 1224 out of 1312 records (93.3%) were classified under at least one research theme. The total number of publications associated with each theme and their percentage contributions during the three research phases were calculated and presented in Section 3.4. The ten most-cited publications listed in Section 3.3 were also classified according to these themes.

Third, the identified research themes were linked to the corresponding sections of the critical literature review (Section 3.4). Research themes that consistently accounted for a substantial proportion of publications were considered established areas, while those showing increasing research activity or relatively fewer publications were examined as emerging areas with potential opportunities for further investigation. This approach establishes a connection between the bibliometric findings and the scientific developments discussed in the review.

3. Results of the Bibliometric Analysis

3.1. Annual Publications Between 2005 and 2026

The annual publication trend in TWIP-steel research in Figure 3 from 2005 to 2026 reveals a substantial expansion of scientific interest over the past two decades. Publication output increased from only 2 papers in 2005 to 92 in 2012, followed by sustained activity with prominent peaks of 104 publications in 2015 and 101 in 2018. Although some fluctuations are observed in the subsequent years, the field continues to maintain a considerable research output. The three-year trailing moving average further highlights the rapid growth phase up to around 2017–2018, followed by a gradual moderation in publication activity. On the basis of the annual output, three research phases can be distinguished. Phase I (2005–2011) was a period of emergence, in which annual output increased from 2 to 61 records; it accounts for 194 records (14.8% of the corpus). Phase II (2012–2018) was a period of expansion, in which annual output remained between 81 and 104 records; with 632 records (48.2%), or about 90 records per year, it is the most productive period of TWIP-steel research. Phase III (2019–2026) is a period of consolidation, in which no complete year exceeded 78 records; it contains 486 records (37.0%), and its mean output for the complete years 2019–2025 (about 64 records per year) is approximately 29% lower than that of Phase II. These phases are used in Section 3.4 to follow how the research themes developed over time.

3.2. Prolific Nations

The extent of international research networking and collaboration in the TWIP-steel domain is illustrated in Figure 4 generated with the aid of VOSviewer through a country level co-authorship network. Different colors represent distinct collaboration clusters, while the connecting lines indicate research linkages between countries. The size of each node reflects the relative publication contribution of the corresponding country, whereas the thickness of the connecting lines represents the strength of collaboration between them. Larger nodes such as China, Germany, South Korea, and the United States indicate comparatively higher research activity, while the dense interconnections among several countries demonstrate the increasingly collaborative and international nature of TWIP-steel research. Publications on TWIP alloys originate from 48 countries. The most productive nations are listed in Table 2. China leads decisively with 492 documents (37.5% of the total), ahead of South Korea with 222 (16.92%) and Germany with 180 (13.71%). The United States and Australia follow, contributing 6.25% and 5.64%, respectively.

Figure 5 presents the density visualization map of highly cited countries generated using VOSviewer. South Korea received the highest number of citations (12,380), followed by China (11,278) and Germany (9570), highlighting their substantial contributions to TWIP-steel research. China led in publication output with 492 documents (37.5%), followed by South Korea with 222 (16.92%) and Germany with 180 (13.71%). The United States and Australia received 5137 and 3707 citations, respectively, while Iran, the United Kingdom, and Spain received 2449, 2340, and 2336 citations, respectively.

The analysis reveals notable differences between publication output and citation impact across countries. To assess the research impact relative to publication output, the total citations of each country in Table 2 were divided by its corresponding number of publications. Among the 21 countries with at least 20 publications, France recorded the highest average citations per document (113.6), followed by Belgium (76.7), the Russian Federation (75.0), and the Netherlands (72.2). The United States (62.6), Hong Kong (58.6), South Korea (55.8), and Germany (53.2) also demonstrated relatively high citation averages. In contrast, China, despite having the highest number of publications, recorded an average of 22.9 citations per document. Furthermore, the three most productive countries collectively contributed publication counts equivalent to 68.1% of the total dataset, indicating that TWIP-steel research

is concentrated in a relatively small number of countries. Since publications involving international collaborations were counted separately for each participating country, this percentage does not represent the proportion of unique publications. It is also important to consider that citation counts are influenced by the publication year, as recently published studies have had less time to accumulate citations. Therefore, differences in the average citation impact across countries may partly reflect variations in the publication periods of their research output.

3.3. Citation Landscape of Documents

Table 3 presents the ten most highly cited documents in TWIP-steel research, based on citation data retrieved from the Scopus database as of 17 September 2026. The most highly cited publication is Twinning-Induced Plasticity (TWIP) Steels [24] by De Cooman et al., with 1552 citations. This work provides a comprehensive overview of the fundamental characteristics of TWIP steels, with particular emphasis on their exceptional combination of strength and ductility, deformation mechanisms, microstructural evolution, and strain-hardening behaviour. The second most highly cited publication is High Manganese Austenitic Twinning Induced Plasticity Steels: A Review of the Microstructure–Properties Relationships by Bouaziz et al. [25], with 1439 citations. The study extensively reviews the relationship between microstructure and mechanical properties in high-Mn TWIP steels, addressing important aspects such as plastic deformation mechanisms, strain hardening, yield strength, crystallographic texture, fracture behaviour, and fatigue. The third most highly cited publication, with 877 citations, is Dislocation and Twin Substructure Evolution During Strain Hardening of an Fe–22 wt.%; Mn–0.6 wt.% C TWIP Steel Observed by Electron Channelling Contrast Imaging [26] by Gutierrez-Urrutia and Raabe. The authors investigated the progressive evolution of dislocation and twin substructures during tensile deformation. At low strains, below approximately 0.1 true strain, rapid development of the dislocation substructure was associated with a high strain-hardening rate. At intermediate strains, deformation twinning progressively reduced the effective dislocation mean free path, thereby enhancing dislocation storage and strain hardening. However, at higher strains the capability for further refinement of the dislocation and twin substructures became increasingly limited, resulting in a gradual reduction in strain-hardening capacity. The remaining highly cited documents further extend this foundation by examining the roles of stacking-fault energy, temperature, strain rate, grain size, crystallographic orientation, grain and twin boundaries, alloy chemistry, low-density Fe–Al–Mn–C alloy design, and deformation-induced microstructural changes in governing the tensile response and strain-hardening behaviour of TWIP steels. The ten most-cited publications were published between 2008 and 2018, corresponding to Phases I and II identified in Section 3.1, and collectively received 8615 citations. An examination of these publications reveals that their research contributions are mainly concentrated in a few key areas of TWIP-steel research. Among them, four publications [24–27] primarily focused on stacking fault energy, deformation twinning, and strain-hardening mechanisms, while one study [28] investigated the influence of grain size, crystallographic orientation, and grain and twin boundaries on mechanical behaviour. One publication [29] addressed alloy composition and the development of low-density Fe–Mn–Al–C steels, while another study [30] examined the influence of grain size, crystallographic orientation, and grain and twin boundaries on mechanical behaviour. The remaining three publications [31–33] focused on stacking fault energy, deformation twinning, and strain-hardening mechanisms [31,32], as well as alloy composition and the development of low-density Fe–Mn–Al–C steels [33].Notably, none of the ten most-cited publications primarily focused on service-related properties, such as hydrogen embrittlement, fatigue behaviour, fracture mechanisms, or weldability. Similarly, studies in-

volving ML and other data-driven approaches were absent from this group. These findings indicate that the most highly cited research during the earlier phases was largely centred on understanding the fundamental deformation mechanisms, microstructural characteristics, and alloy development of TWIP steels.

Table 3. Ten most highly cited publications.

Rank	Document Name	Citations	Authors
1	Twinning-induced plasticity (TWIP) steels [24]	1552	De Cooman B.C.; Estrin Y.; Kim S.K.
2	High manganese austenitic twinning induced plasticity steels: A review of the microstructure properties relationships [25]	1439	Bouaziz O.; Allain S.; Scott C.P.; Cugy P.; Barbier D.
3	Dislocation and twin substructure evolution during strain hardening of an Fe–22 wt.% Mn–0.6 wt.% C TWIP steel observed by electron channelling contrast imaging [26]	877	Gutierrez-Urrutia I.; Raabe D.
4	Dependence of tensile deformation behavior of TWIP steels on stacking fault energy, temperature and strain rate [27]	869	Curtze S.; Kuokkala V.-T.
5	Effect of grain and twin boundaries on the hardening mechanisms of twinning-induced plasticity steels [28]	810	Bouaziz O.; Allain S.; Scott C.
6	Current state of Fe–Mn–Al–C low density steels [29]	803	Chen S.; Rana R.; Haldar A.; Ray R.K.
7	The effect of grain size and grain orientation on deformation twinning in a Fe–22 wt.% Mn–0.6 wt.% C TWIP steel [30]	735	Gutierrez-Urrutia I.; Zaefferer S.; Raabe D.
8	Revealing the strain-hardening behavior of twinning-induced plasticity steels: Theory, simulations, experiments [31]	538	Steinmetz D.R.; Jäpel T.; Wietbrock B.; Eisenlohr P.; Gutierrez-Urrutia I.; Saeed-Akbari A.; Hickel T.; Roters F.; Raabe D.
9	The influence of stacking fault energy on the microstructural and strain-hardening evolution of Fe–Mn–Al–Si steels during tensile deformation [32]	498	Pierce D.T.; Jiménez J.A.; Bentley J.; Raabe D.; Wittig J.E.
10	Fe–Al–Mn–C lightweight structural alloys: A review on the microstructures and mechanical properties [33]	494	Kim H.; Suh D.-W.; Kim N.J.

3.4. Evolution of the Research Themes and Framework for the Review

The research phases provide an overview of publication trends over time, while the identified research themes highlight the major areas of scientific investigation in TWIP steels. Table 4 presents the seven research themes, their corresponding publication counts, and their percentage contributions across the three research phases.

Among the seven themes, the highest publication contributions were observed in areas related to deformation mechanisms, thermomechanical processing, and alloy development. Theme B (thermomechanical processing and microstructure) emerged as the most extensively studied area, comprising 688 publications (52.4% of the total dataset). Its contribution increased from 48.3% in Phase II to 57.4% in Phase III, indicating growing research interest in processing techniques and microstructural development. Theme A (stacking fault energy, deformation twinning, and strain hardening) accounted for 591 publications (45.0%). How-

ever, its share gradually declined from 49.5% in Phase I to 43.8% in Phase III. This reduction may indicate a gradual transition from investigating fundamental deformation mechanisms towards applying these concepts to alloy development and processing optimisation. The importance of this theme is further reflected in Table 3, where six of the ten most-cited publications belong to Theme A, collectively receiving 5773 citations, representing 67.0% of the citations received by the ten publications. Similarly, Theme C (alloy chemistry and alloy design) included 346 publications (26.4%), with its contribution increasing from 21.6% in Phase I to 29.0% in Phase III, reflecting continued interest in developing TWIP steels with improved mechanical properties through compositional modifications.

Table 4. Research themes of the TWIP-steel corpus and their evolution across the three research phases. Themes were assigned by rule-based coding of titles, abstracts and author keywords, and a record may belong to several themes. Records (%): number of records and share of the corpus; Phase I/II/III (%): share of the records of each phase (Phase I: 2005–2011, 194 records; Phase II: 2012–2018, 632 records; Phase III: 2019–2026, 486 records); Section: section of this review in which the theme is discussed.

Theme	Records (%)	Phase I/II/III (%)	Section
A. SFE, deformation twinning and strain hardening	591 (45.0)	49.5/44.6/43.8	Section 4.1
B. Thermomechanical processing and microstructure	688 (52.4)	53.6/48.3/57.4	Sections 4.2.1–4.2.6
C. Alloy chemistry and alloy design	346 (26.4)	21.6/25.8/29.0	Sections 4.1.2, 4.2.7 and 7
D. Hydrogen embrittlement	91 (6.9)	2.1/6.3/9.7	Sections 4.3 and 7
E. Fatigue and fracture	204 (15.5)	10.8/12.3/21.6	Sections 4.4, 5.3, 5.4 and 7
F. Machine learning and data-driven design	7 (0.5)	0.5/0.0/1.2	Sections 5 and 7
G. Physics-based computational modelling	87 (6.6)	2.6/6.2/8.8	Sections 4.1.2 and 7

Although the themes related to service performance and computational approaches contributed fewer publications, their relative contributions increased considerably over the three research phases. Theme D (hydrogen embrittlement) comprised 91 publications, with its share increasing from 2.1% in Phase I to 6.3% in Phase II and 9.7% in Phase III. Similarly, Theme E (fatigue behaviour and fracture mechanisms) included 204 publications, with its contribution doubling from 10.8% in Phase I to 21.6% in Phase III. Theme G (physics-based computational modelling) accounted for 87 publications, and its share increased from 2.6% to 8.8% over the same period. These trends indicate increasing research attention towards the service performance, structural reliability, and computational investigation of TWIP steels. Interestingly, none of these themes was represented among the ten most-cited publications listed in Table 3. However, this observation should not be interpreted as an indication of lower scientific significance, since relatively recent publications have had less time to accumulate citations compared with earlier studies.

In comparison, Theme F (ML and data-driven design) remained the least explored research area, with only seven publications, representing approximately 0.5% of the total dataset. The earliest of these was the artificial neural network (ANN) study of Dini et al. (2009) [10], which predicted the tensile properties of Fe–Mn–(Al, Si) TRIP/TWIP steels from their chemical composition. No Theme F publication appeared during Phase II, and the remaining publications were all published between 2022 and 2026. Thus, although ML was first applied to TWIP steels during Phase I, sustained research activity in this area emerged only in Phase III, indicating that the application of ML techniques in TWIP-steel research is still at an early stage. Although Phase III recorded lower annual publication output than Phase II (Figure 3), the relative contributions of studies focusing on service-

related properties, computational modelling, and data-driven approaches increased. This suggests that TWIP-steel research is gradually expanding beyond fundamental deformation mechanisms towards performance evaluation, predictive modelling, and the development of application-oriented materials.

The findings of the thematic analysis also provide a systematic basis for organising the critical literature review, as indicated in the final column of Table 4. Themes A and C address the influence of alloy composition, austenite stability, stacking fault energy, and deformation mechanisms. Theme B focuses on thermomechanical processing and the resulting microstructural characteristics, while Themes D and E examine service-related properties, including hydrogen embrittlement, fatigue behaviour, and fracture mechanisms. Themes F and G represent the application of data-driven methods and physics-based computational modelling, respectively, which can contribute to the prediction of material behaviour and the optimisation of alloy composition and processing conditions.

4. Discussion: Critical Review of the Bibliometrically Identified Research Themes

This section discusses the results of Section 3 by reviewing the established research themes listed in Table 4. The review begins with Theme A, which contains most of the highly cited literature, continues with Themes B and C, which together form the largest and a steadily growing part of the literature, and ends with the service-related themes: Theme D and Theme E.

A TWIP-steel alloy schema that summarizes the sequential relationship between alloy chemistry, processing, microstructure, deformation mechanisms, strain hardening, and final performance has been illustrated in Figure 6. The chemical composition, particularly Mn, C, Al, and Si, governs austenite stability through parameters such as stacking fault energy and the $\gamma \rightarrow \varepsilon$ transformation tendency. Subsequent thermomechanical processing modifies the grain structure, texture and phase distribution which in turn influences the activation of deformation mechanisms such as slip, TWIP, TRIP, DSA (Dynamic Strain Aging), and PLC (Portevin–Le Chatelier) behaviour [34]. These mechanisms control dislocation accumulation and deformation twinning, thereby determining the strain-hardening response and ultimately the strength, ductility, fatigue resistance, and corrosion-related behaviour of TWIP steels [1]. The feedback pathway further emphasizes that experimentally observed performance can be used to refine alloy chemistry and processing conditions for improved material design.

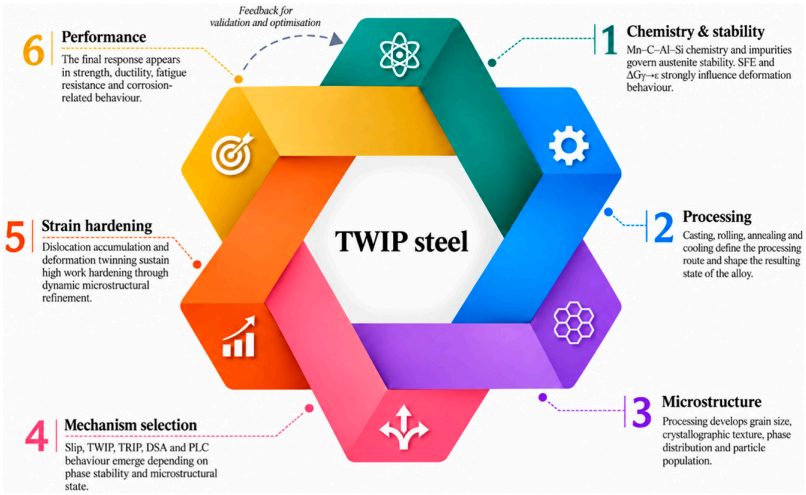


Figure 6. TWIP-steel alloy–process–property schema.

4.1. Fundamental Characteristics and Deformation Mechanisms of TWIP Steels

This section corresponds to Theme A, which represents one of the most established research areas in TWIP steels. It focuses on the role of stacking fault energy (SFE) in determining the dominant deformation mechanisms, including dislocation glide, deformation twinning, and ε-martensite formation [27,32].

4.1.1. Crystallographic Basis and the Stacking-Fault-Energy Criterion

SFE is among the most influential parameters controlling the deformation response of high-Mn austenitic steels. In a FCC crystal, atoms on the close-packed (111) planes ideally follow an ABCABCABC... stacking sequence. Plastic deformation locally disturbs this regular sequence and produces a stacking fault as shown in Figure 7. Because the atomic arrangement within an intrinsic stacking fault resembles a very thin region of hexagonal close-packed (HCP) structure which has a sequence of ABABAB..., the fault can, from a thermodynamic standpoint, be regarded as an extremely thin platelet of ε-martensite embedded within the γ-austenitic matrix. This interpretation forms the basis of most thermodynamic models subsequently developed for TWIP and TRIP steels [34,35].

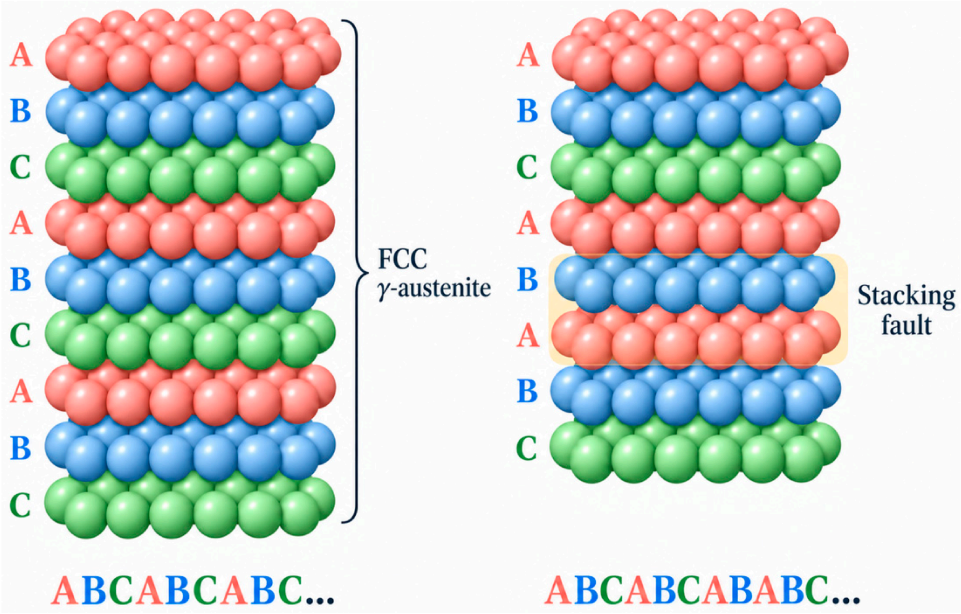


Figure 7. Schematic representation of the FCC stacking sequence and intrinsic stacking-fault formation in γ-austenite where A, B, and C denote three distinct atomic stacking positions.

The importance of SFE originates from its ability to alter the stability and separation of Shockley partial dislocations and, consequently, the relative ease of dislocation glide, deformation twinning and strain-induced martensitic transformation. Allain et al. established one of the most frequently adopted frameworks for Fe–Mn–C steels and correlated calculated SFE directly with deformation microstructures. For Fe–22Mn–0.6C steel, they reported approximately 80 mJ/m^2 at 673 K, where dislocation glide dominated; approximately 19 mJ/m^2 at 293 K, where dislocation glide and mechanical twinning coexisted; and approximately 10 mJ/m^2 at 77 K, where ε-martensitic transformation accompanied glide. This experimentally supported connection between SFE and deformation mode subsequently became a central concept in the design of TWIP steels [34].

4.1.2. Thermodynamic Description of SFE

The classical thermodynamic treatment assumes that an intrinsic stacking fault corresponds approximately to a two-atomic-layer-thick HCP region. The SFE [34], Γ, can therefore be represented in Equation (1):

$$\Gamma = 2\rho\Delta G^{\gamma\to\varepsilon} + 2\sigma^{\gamma/\varepsilon} \quad (1)$$

where ρ is the molar surface density of atoms on the close-packed (111) plane, $\Delta G^{\gamma\to\varepsilon}$ is the molar Gibbs free-energy difference associated with the transformation of FCC γ-austenite to HCP ε-martensite, and $\sigma^{\gamma/\varepsilon}$ is the interfacial energy between the two phases [34]. The first term in Equation (1) represents the thermodynamic energy required to create the local ε-like arrangement, while the second represents the energetic cost of the two γ/ε interfaces bounding that region. SFE is therefore controlled not only by crystallography but also by the relative thermodynamic stability of austenite and ε-martensite. The molar surface density is geometrically related to the FCC lattice parameter a_γ (Equation (2)):

$$\rho = \frac{4}{\sqrt{3}\,a_\gamma^2 N_A} \quad (2)$$

where N_A is Avogadro's number. Allain et al. used an approximately constant lattice parameter of 0.361 nm for the Fe–Mn–C compositional range considered [34]. A more general representation of the free-energy difference is given by Equation (3):

$$\Delta G^{\gamma\to\varepsilon} = \Delta G^{\gamma\to\varepsilon}_{\text{chem}} + \Delta G^{\gamma\to\varepsilon}_{\text{mag}} + \Delta G^{\gamma\to\varepsilon}_{\text{seg}} + \Delta G_{\text{ex}} \quad (3)$$

where the four terms respectively describe the chemical contribution, the contribution of magnetic ordering, segregation or the Suzuki effect, and additional excess energy arising, for example, from grain-size effects. Zambrano incorporated these terms into extended SFE maps for Fe–Mn–Al–C–Si steels [36].

For a multicomponent alloy, the chemical contribution may conveniently be expressed as Equation (4):

$$\Delta G^{\gamma\to\varepsilon}_{\text{chem}} = \sum_i x_i \Delta G_i^{\gamma\to\varepsilon} + 1/2 \sum_{i<j} x_i x_j \Delta\Omega_{ij}^{\gamma\to\varepsilon} \quad (4)$$

where x_i is the mole fraction of component i, $\Delta G_i^{\gamma\to\varepsilon}$ is the corresponding transformation free energy of the pure component, and $\Delta\Omega_{ij}^{\gamma\to\varepsilon}$ represents binary interaction terms [37]. This form allows the influences of Fe-Mn, Fe-C, Mn-C, Fe-Al, Fe-Si and other interactions to be incorporated into the calculated SFE.

Allain et al. initially developed this approach for Fe–Mn–C, while Dumay et al. extended it to additional alloying elements such as Al, Si, Cu and Cr. Dumay et al. found that Al strongly increases SFE, Cu also raises it while markedly reducing the Néel temperature, Cr decreases SFE, and Si produces a more complicated response [38].

Nakano and Jacques refined this type of CALPHAD (CALculation of PHAse Diagrams), treatment by reassessing the thermodynamic parameters of the HCP phase. Their analysis showed that one internally consistent parameter set could reproduce phase-equilibrium information, T_0 temperatures and the compositional and temperature dependence of the SFE. They further observed that the SFE is particularly temperature-sensitive in the paramagnetic state and comparatively Mn-sensitive in the antiferromagnetic state [39].

For a subregular solution, the excess term may be represented through a Redlich–Kister-type expansion (Equation (5)):

$$G^{\phi}_{\text{ex}} = \sum_{i<j} x_i x_j \sum_k L^{\phi}_{ij,k} \left(x_i - x_j\right)^k \quad (5)$$

where $L_{ij,k}{}^{\varphi}$ represents the binary interaction parameters of phase φ. This allows the interaction coefficients themselves to vary with composition and temperature [40].

Magnetic Contribution

Magnetism is particularly important in Fe–Mn alloys because both austenite and ε-martensite may undergo magnetic-ordering transitions. The magnetic contribution is commonly represented using the Inden–Hillert–Jarl formalism in Equation (6):

$$G_{\mathrm{mag}}^{\phi} = RT\ln(\beta^{\phi}+1)f(\tau^{\phi}) \tag{6}$$

with

$$\tau^{\phi} = \frac{T}{T_N^{\phi}} \tag{7}$$

where β^{φ} represents the magnetic moment and $T_N{}^{\varphi}$ is the Néel temperature [27].

For Fe–Mn–C-containing alloys, commonly employed approximations include

$$\frac{\beta^{\gamma}}{\mu_B} = 0.7x_{\mathrm{Fe}} + 0.62x_{\mathrm{Mn}} - 0.64x_{\mathrm{Fe}}x_{\mathrm{Mn}} - 4x_{\mathrm{C}} \tag{8}$$

and

$$\frac{\beta^{\varepsilon}}{\mu_B} = 0.62x_{\mathrm{Mn}} - 4x_{\mathrm{C}} \tag{9}$$

together with

$$T_N^{\varepsilon} = 580x_{\mathrm{Mn}} \tag{10}$$

These magnetic contributions help explain why a simple chemical-energy model cannot always reproduce experimentally observed trends in SFE [37]. This is particularly evident in the studies of Tian and co-workers. For Fe–Mn–Al–C alloys, they observed a nonlinear response of SFE to Al and related the discrepancy between purely thermodynamic and experimentally determined SFE to the magnetic state and the anomalous variation in shear modulus associated with antiferromagnetic ordering [41]. Similarly, another Fe–Mn–Si–C work showed that Si modifies the SFE through both chemical and magnetic routes, including changes in localized magnetic moment, Néel temperature and shear modulus [42].

Ideal and Effective SFE

An important refinement is the distinction between an ideal stacking fault, assumed infinitely extended and free from the elastic influence of bounding partial dislocations, and a real or effective stacking fault. Curtze and Kuokkala expressed the latter as in Equation (11):

$$\Gamma^{*} = 2\rho\Delta G^{\gamma\to\varepsilon} + 2\sigma^{\gamma/\varepsilon} + 2s\Delta G_S \tag{11}$$

where s is the spacing between close-packed planes and ΔG_S represents strain energy associated with the actual fault configuration [27]. For two parallel partial dislocations, the strain-energy contribution can be approximated in Equation (12):

$$\Delta G_S = \frac{\mu\varepsilon^2}{4(1-\nu)} \tag{12}$$

where μ is shear modulus, ε is the normal strain and ν is Poisson's ratio [27]. This distinction is essential because experimentally observed stacking faults are bounded by dislocations and therefore do not necessarily correspond exactly to the ideal thermodynamic state [35]. Nakano and Jacques in Equation (13) similarly expressed the SFEs of a fault containing n HCP planes as

$$\Gamma = n\rho\left(\Delta G^{\mathrm{fcc}\to\mathrm{hcp}} + \Delta G_{\mathrm{strain}}\right) + n\sigma(n) \tag{13}$$

with $n = 2$ for an intrinsic stacking fault. Their treatment emphasizes that uncertainties in the interfacial energy and strain contribution can produce sizeable differences between calculated SFE values even for the same nominal alloy composition [39]. Pierce et al.

provided an important experimental refinement by explicitly separating coherency-strain energy from measured SFEs. They expressed the ideal SFE as Equation (14):

$$\Gamma_1 = \Gamma_{exp} - n\rho E_{str} \quad (14)$$

where E_{str} accounts for coherency strain generated because the HCP-like stacking-fault region has a slightly different volume from the surrounding FCC lattice [43].

Using weak-beam TEM, Pierce et al. measured SFEs of approximately 15 ± 3, 21 ± 3, and 39 ± 5 mJ/m^2 for Fe–22Mn–3Al–3Si, Fe–25Mn–3Al–3Si and Fe–28Mn–3Al–3Si, respectively. After removal of the coherency contribution, the corresponding ideal values were approximately 14 ± 3, 19 ± 3 and 35 ± 5 mJ/m^2. They further found γ/ε interfacial energies of about 8–12 mJ/m^2 for the investigated TRIP/TWIP steels, compared with substantially larger values in binary Fe–Mn alloys ranging from 15–33 mJ/m^2 [43].

Their results also suggested that $\sigma^{\gamma/\varepsilon}$ should not always be treated as a universal constant. An empirical description was proposed (Equation (15)) in which interfacial energy changes approximately parabolically with the thermodynamic free-energy difference:

$$\sigma^{\gamma/\varepsilon} = c\left[2\rho\left(\Delta G_{chem}^{\gamma\to\varepsilon} + \Delta G_{mag}^{\gamma\to\varepsilon}\right)\right]^2 + \sigma_{min}^{\gamma/\varepsilon} \quad (15)$$

with a fitted minimum interfacial energy near 9.5 mJ/m^2 and $c = 0.01$ m^2/mJ [43]. Zambrano subsequently incorporated this idea into his wider SFE-map analysis, while also noting that its quantitative applicability remains alloy dependent [36].

The Effect of Austenite Grain Size

SFE is also influenced by microstructural scale. Saeed-Akbari et al. showed through composition-dependent, SFE maps that increasing temperature and Al content shifts the SFE upward, whereas increasing austenite grain size can reduce it. Their calculations further suggested that the effects of temperature and Al are strongest in lower-Mn steels [44].

Zambrano introduced an explicit grain-size contribution in Equation (16):

$$\Delta G_{ex} = 170.06\exp\left(-\frac{d}{18.55}\right) \quad (16)$$

where d is the austenite grain size in μm [36].

This term becomes increasingly salient as the grain size enters the fine-grained regime. Consequently, SFE should not always be interpreted purely as a composition-dependent bulk property; thermomechanical processing that substantially modifies grain size can alter the apparent or effective faulting behaviour. The importance of this issue is further demonstrated after friction-stir welding. Lee et al. measured and calculated SFE for Fe–18Mn–0.6C, Fe–18Mn–0.6C–1.5Al and Fe–30Mn–3Al–3Si steels before and after FSW. SFE increased from 13.0 to 27.4 mJ/m^2, from 29.0 to 34.4 mJ/m^2, and from 54.4 to 68.0 mJ/m^2, respectively, demonstrating that the defect structure and grain refinement generated by processing must be considered in addition to nominal composition [45].

4.1.3. Experimental Determination of SFE from Shockley Partial-Dislocation Separation

The thermodynamic description can be independently examined through the equilibrium configuration of dissociated dislocations. A perfect FCC dislocation may dissociate into two Shockley partial dislocations separated by a stacking-fault ribbon. The partial dislocations repel each other elastically, whereas the fault energy attempts to reduce the area of the ribbon and therefore pulls the two partials towards one another. Their equilibrium separation is accordingly determined by the balance between these opposing forces.

For the commonly employed isotropic approximation (Equation (17)):

$$d = \frac{Gb_p^2}{8\pi\Gamma}\left(\frac{2-\nu}{1-\nu}\right)\left[1 - \frac{2\nu\cos(2\theta)}{2-\nu}\right] \quad (17)$$

where d is the separation of the Shockley partials, G is the shear modulus, b_p is the magnitude of their Burgers vector, ν is Poisson's ratio, and θ describes the character of the dislocation [46].

The central physical relationship is therefore presented in Equation (18):

$$d \propto \frac{1}{\Gamma} \tag{18}$$

so that decreasing SFE produces a wider separation of the partial dislocations and a broader stacking-fault ribbon. Kim and De Cooman used this weak-beam dark-field TEM approach to obtain an SFE of approximately 30 ± 10 mJ/m^2 for Fe–18Mn–0.6C–1.5Al. They also found unusually large separations for some screw dislocations and related them to interactions between partial-dislocation strain fields and C-containing point-defect complexes [46].

This observation is important because Equation (17) assumes an equilibrium configuration governed primarily by elastic repulsion and fault energy. Solute-dislocation interactions can therefore introduce scatter into experimentally inferred SFE values.

The same approach was subsequently employed to quantify the effect of Al. Kim, Lee and De Cooman measured approximately 13 ± 3 mJ/m^2 for Fe–18Mn–0.6C and found an experimental increase of roughly 11.3 mJ/m^2 per 1 wt.% Al addition. This increase explains the delayed development of twins and the reduced strain-hardening response observed when the Al concentration is increased [47].

Applied stress further alters the partial separation. Park et al. expressed this effect approximately as Equation (19):

$$d_{SP} = \frac{1}{8\pi}\left(\frac{2-3\nu}{1-\nu}\right)\frac{Gb_{SP}^2}{\Gamma_{SF} - \tau b_{SP}/2} \tag{19}$$

which gives the ideal limiting stress for infinite separation as (Equation (20)):

$$\tau_{crit} = \frac{2\Gamma_{SF}}{b_{SP}} \tag{20}$$

An increase in stacking fault energy (SFE) generally increases the stress required for deformation-twin formation. However, Park et al. observed that twinning started at lower stresses than those predicted by a simple force-balance model. This indicates that SFE is not the only factor governing twin nucleation. The authors suggested that short-range ordering of alloying elements can promote glide-plane softening, allowing dislocations to move more easily along specific slip planes. As a result, planar dislocation glide occurs before twinning and can facilitate the formation of deformation twins even at comparatively lower stresses [48].

4.1.4. Determination of SFE by X-Ray Diffraction

X-ray diffraction provides another widely used route for obtaining SFE from stacking-fault probability and microstrain. One commonly adopted Schramm–Reed-type expression is presented in Equation (21):

$$\Gamma = \frac{K_{111}\omega_0 G_{111} a_0 A^{-0.37}}{\sqrt{3}\pi}\,\frac{\langle \varepsilon_{50}^2 \rangle_{111}}{\alpha} \tag{21}$$

where $K_{111}\omega_0 = 6.6$, a_0 is the lattice parameter, α is the stacking-fault probability, and

$$A = \frac{2C_{44}}{C_{11} - C_{12}} \tag{22}$$

is the Zener elastic-anisotropy parameter (Equation (22)), while

$$G_{111} = \frac{C_{44} + C_{11} - C_{12}}{3} \tag{23}$$

is the shear modulus relevant to the ⟨111⟩ direction presented in Equation (23) [48].

Castañeda et al. emphasized a major limitation of this approach: the resulting SFE is highly sensitive to the elastic constants selected. In their Fe–Mn–Al–C assessment, uncertainty in these constants could produce SFE errors of up to approximately 37%, sufficiently large in some cases to affect the inferred deformation mechanism [48]. Thus, disagreement between TEM-, XRD- and thermodynamics-derived SFE values should not automatically be interpreted as experimental failure; the techniques evaluate the fault state through different physical quantities and carry different sources of uncertainty.

The XRD method was also applied by Peng et al. to Fe–20Mn–3Cu–*x*C steels. Increasing C from approximately 0.23 to 1.41 wt.% decreased stacking-fault probability and increased the calculated SFE from approximately 22.4 to 29.6 mJ/m^2 [49].

4.1.5. Temperature and Strain-Rate Dependence

Temperature alters SFE primarily through the temperature dependence of $\Delta G^{\gamma\to\varepsilon}$ and the magnetic states of γ and ε. Thus, the same chemical composition may exhibit TRIP-, TWIP- or slip-dominated behaviour depending upon testing temperature. Curtze and Kuokkala investigated three TWIP steels with room-temperature SFEs ranging from approximately 20.5 to 42 mJ/m^2 over temperatures between −50 and 80 °C and strain rates extending from quasi-static conditions (10^{-3} s^{-1}) to approximately 1250 s^{-1}. Using split-Hopkinson tensile bar experiments under dynamic loading, they observed considerable variations in tensile strength, ductility, and strain-hardening behaviour with temperature and strain rate. Their thermodynamic calculations indicated that increasing the initial testing temperature to 80 °C increased the SFE by approximately 4–5 mJ/m^2 for the investigated alloys. Furthermore, considering that approximately 90% of the plastic deformation work is converted into heat, they estimated an adiabatic temperature rise of approximately 95 °C during high-strain-rate deformation, potentially increasing the SFE by up to 25 mJ/m^2. Experimentally, a pronounced reduction in tensile elongation was observed at elevated temperatures and high strain rates, which the authors attributed to the combined effects of the higher initial SFE and adiabatic heating during deformation. These findings suggest that the temperature rise associated with dynamic deformation can substantially modify the instantaneous SFE, potentially favouring dislocation slip over mechanical twinning and thereby reducing the contribution of the TWIP effect to strain hardening and ductility [27]. The subsequent multicomponent thermodynamic model of Curtze et al. [27] extended this description to Fe–Cr–Ni–Mn–Al–Si–Cu–C–N alloys and explicitly incorporated chemical interactions, magnetic contributions and interstitial nitrogen [35]. Consistent with these findings of Curtze et al. [27], Wang et al. (2022) [50] investigated the tensile deformation behaviour of TWIP steel over strain rates ranging from 0.001 to 3000 s^{-1}, reporting an increase in yield strength from 190 MPa under quasi-static loading to 770 MPa under dynamic loading. Although high strain rates promoted earlier twin initiation and enhanced strain hardening during the initial stages of deformation, an estimated adiabatic temperature rise of approximately 117 °C increased the calculated SFE from 30.1 to 52.6 mJ/m^2. This temperature-induced increase in SFE was associated with a reduced growth rate of twin boundary fraction and a subsequent decline in strain-hardening rate at larger strains, despite continued twin development. Hokka et al. (2008) [51] reported distinct strain-rate sensitivities under tensile and compressive loading, with Fe–28Mn–1.58Al–0.28Si–0.076C steel exhibiting higher sensitivity in tension at quasi-static strain rates, whereas the Nb-containing Fe–25Mn–1.62Al–0.24Si–0.084C–0.052Nb and Fe–27Mn–4.14Al–0.52Si–0.068C–0.048Nb steels showed greater sensitivity in compression. Under dynamic loading, a pronounced increase in tensile strain-rate sensitivity occurred at approximately 750 s^{-1}, whereas a comparable transition appeared at higher strain rates

during compression for the Nb-containing alloys. The differences were suggested to arise partly from variations in the active twinning systems and specimen orientations relative to the rolling direction. Xu and co-workers investigated intermediate-rate tensile deformation ($0.001–400\ s^{-1}$) and observed an overall increase in tensile strength and strain-hardening response with increasing strain rate, although the strength response was not strictly monotonic at low rates [52]. Kang and team further reported an increase in tensile strength from 1048 MPa under quasi-static loading to 1171 MPa at $1500–2000\ s^{-1}$, while elongation remained nearly unchanged (61% and 59%, respectively) [53].

4.1.6. Deformation Mechanisms in TWIP Steels

The exceptional strength–ductility combination of TWIP steels originates from the concurrent operation and progressive interaction of dislocation glide and deformation twinning within the FCC austenitic matrix [54]. Prior to deformation processing, TWIP steels are commonly subjected to homogenization treatment to minimize chemical segregation and establish a more uniform alloy composition throughout the microstructure [55].

Figure 8a,b presents the optical micrographs of the homogenized Fe–22Mn–3Al–3Si–0.01C steel under different magnifications. The specimen was prepared following standard metallographic procedures, etched with a 10% Nital solution, and examined using a Carl Zeiss AXIOVERT 40 MAT optical microscope (Carl Zeiss, Oberkochen, Germany). Prior to deformation, the alloy was homogenized at 1100 °C to reduce chemical segregation and promote compositional uniformity. The microstructure is predominantly composed of equiaxed austenitic grains with clearly defined grain boundaries and twins.

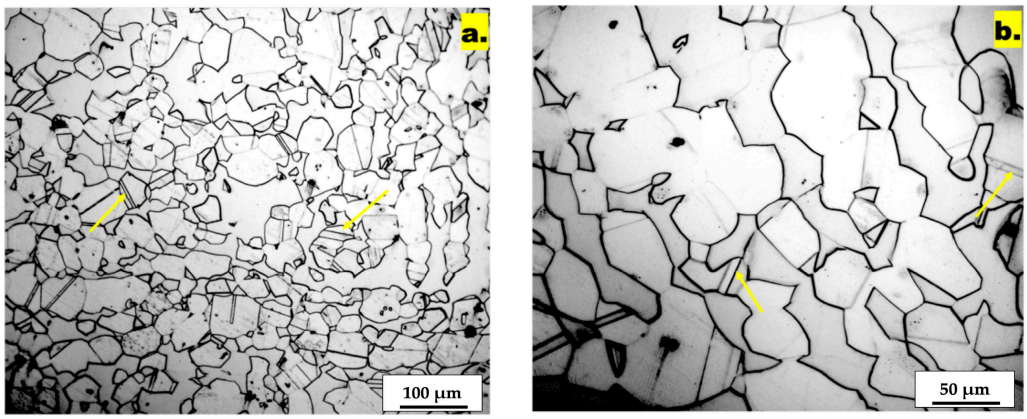


Figure 8. Optical micrographs of homogenised Fe–22Mn–3Al–3Si–0.01C steel showing twins in the austenitic microstructure, indicated by yellow arrows under different magnifications of (**a**) 20× and (**b**) 50×.

At the early stages of plastic deformation, strain accommodation is primarily governed by dislocation glide. Owing to the relatively low-to-intermediate SFE of TWIP steels, perfect dislocations readily dissociate into Shockley partial dislocations separated by stacking faults. The reduced tendency for cross-slip promotes planar dislocation motion and facilitates the development of extended stacking faults, which subsequently act as precursors for deformation-twin formation. Allain et al. demonstrated that the coexistence of dislocation glide and mechanical twinning is central to the characteristic work-hardening response of Fe–Mn–C TWIP steels [54]. Mechanical twinning in FCC austenite is associated with the motion of Shockley partial dislocations having Burgers vectors of the type $a/6\langle 112\rangle$ on successive (111) close-packed planes. Bracke et al. experimentally showed that twin activation is closely related to the resolved shear stress acting on the twinning system and demonstrated the applicability of Schmid-type considerations during the initial stage of twinning [56].

Detailed transmission electron microscopy observations by Idrissi et al. further revealed that twin nucleation proceeds through complex dislocation reactions involving overlapping stacking faults and partial dislocations. Their observations indicated that the earliest stage of twin nucleation can be interpreted through pole-type or related mechanisms, whereas subsequent twin thickening is governed by the motion of twinning partials. A high density of sessile Frank dislocations was also observed within the newly formed twins, indicating that deformation twins possess a defect-rich internal structure that can strongly affect both their stability and their interaction with mobile matrix dislocations [57].

More recent in situ TEM studies have provided direct evidence that deformation twins may nucleate through the successive emission of Shockley partial dislocations from grain boundaries. The motion of these partials produces thin twin lamellae whose growth depends strongly on the local stress state. The same observations also showed that stacking faults can impede the motion of twinning partials, while extended dislocations continue to contribute to plastic strain, confirming that dislocation glide, stacking faults and mechanical twinning remain dynamically coupled throughout deformation [58].

As deformation proceeds, the density of the twin lamellae progressively increases and the original austenite grains are subdivided into smaller effective regions. Twin boundaries consequently act as additional barriers to dislocation motion and reduce the effective mean free path of mobile dislocations. This continuous refinement of the deformation substructure gives rise to the titular dynamic Hall–Petch effect, which is widely regarded as a major source of sustained strain hardening in TWIP steels. Allain et al. attributed the high work-hardening rate primarily to the reduction in dislocation mean free path with increasing twin density, while Bouaziz et al. emphasized the combined influence of grain and twin boundaries on isotropic and kinematic hardening [28,54].

The relative contributions of dislocation structures and deformation twins also evolve with strain. Gutierrez-Urrutia and Raabe reported that, at low true strains below approximately 0.1, the developing dislocation substructure itself contributes substantially to strain hardening. At intermediate strains, deformation twinning becomes increasingly important because the newly formed twin boundaries further shorten the dislocation mean free path. However, at high strains the rate of further subdivision of both twin and dislocation structures becomes limited, reducing the capacity for additional dislocation storage and causing the strain-hardening rate to decrease [26]. A similar tendency was observed by Jin and Lee, who showed that the twinned volume fraction initially increases through continuous formation of new deformation twins, whereas a reduction in the twinning rate at large strain is accompanied by a pronounced decrease in strain-hardening capacity [59].

In addition to the direct obstruction of dislocation glide by twin boundaries, twin–dislocation and twin–twin interactions provide further contributions to strengthening. Primary twin boundaries act as effective barriers to mobile dislocations, while the development of secondary twins and their intersections with existing twins generate increasingly complex obstacles to plastic flow. Wang et al. described a three-stage hardening response in which planar dislocation structures dominate initially, primary deformation twinning enhances hardening at intermediate strain, and twin–twin interactions contribute additional strengthening at larger deformation levels [60]. Idrissi et al. further reported that twins in Fe–Mn–C steels are relatively fine and contain high densities of sessile dislocations, suggesting that both dynamic Hall–Petch strengthening and a composite-like strengthening effect arising from defect-rich twin lamellae contribute to the large work-hardening rate [61].

Grain size and crystallographic orientation also strongly influence twin activation. Gutierrez-Urrutia et al. showed that the twinning stress increases as grain size decreases and that, at low strain, twin formation depends strongly on grain orientation in accordance with Schmid-type behaviour. However, at larger strains deformation twins may also appear

in grains that are initially unfavourably oriented for twinning. This deviation was attributed to local stress heterogeneity generated by neighbouring grains, grain boundaries and impinging twin bundles. Such observations demonstrate that twin nucleation is controlled not only by the nominal applied stress but also by the evolving local stress state within the polycrystalline microstructure [30].

At higher strain levels, particularly during severe cold deformation, additional heterogeneous deformation modes may become active. Vercammen et al. observed deformation twinning at relatively low strains in Fe–30Mn–3Al–3Si steel, followed by a progressive increase in twin volume fraction and, at higher deformation levels, the activation of shear-band formation [62]. Thus, the deformation response of TWIP steels can be viewed as an evolving sequence in which dislocation slip is followed by increasing stacking-fault activity, twin nucleation and twin growth, followed by increasingly complex twin–dislocation and twin–twin interactions and, under sufficiently large strains, localized shear deformation.

Dynamic strain aging may operate concurrently with these mechanisms in carbon-containing TWIP steels. Lee et al. associated room-temperature dynamic strain aging with local rearrangement of C-containing point-defect complexes in stacking-fault regions rather than with long-range diffusion of carbon. The same work showed that Al additions can suppress this phenomenon, partly through their influence on stacking fault energy [63]. Temperature further alters the relative contributions of dislocation hardening, twinning and dynamic strain aging, indicating that deformation behaviour is governed by a coupled dependence on composition, stacking fault energy, temperature, strain rate, grain size and local microstructural state [64].

4.2. Thermomechanical Processing and Tensile Behaviour of TWIP Steels

Following the understanding of the role of SFE and the fundamental deformation mechanisms discussed in Theme A, research has progressively focused on controlling the microstructure and mechanical properties of TWIP steels through thermomechanical processing (Theme B) and alloy composition (Theme C). These two research themes are closely related, as both processing conditions and alloying elements influence microstructural evolution and the resulting mechanical behaviour.

The mechanical performance of TWIP steels is strongly governed by their thermomechanical history because cold deformation, recovery, recrystallization, grain growth, phase evolution, precipitation and deformation twinning collectively determine the final strength–ductility balance. Following cold rolling, annealing is carried out to reduce the high density of dislocations, stacking faults and deformation twins generated during deformation and to promote recovery and recrystallization, thereby restoring ductility and controlling the final grain structure and mechanical properties. Consequently, relatively small changes in rolling reduction, annealing temperature or holding time can produce substantial variations in YS, UTS and % El. The schematic in Figure 9 illustrates the evolution of TWIP-steel microstructure from the initial austenitic state through increasing cold deformation, recovery, and partial recrystallization, together with the corresponding changes in twin density, dislocation content, strength, and ductility [63,65].

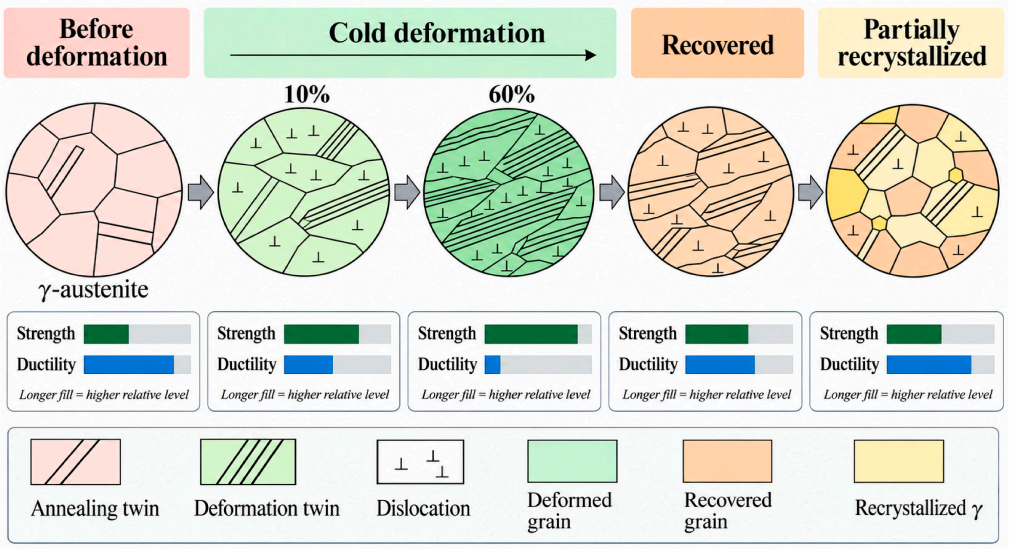


Figure 9. Microstructural evolution and strength–ductility changes during deformation and annealing.

Figure 10 shows the optical micrograph of Fe–22Mn–3Al–3Si–0.01C steel after homogenization at 1100 °C followed by cold rolling to 60% reduction in thickness. The specimen was prepared using standard metallographic procedures, etched with 10% Nital solution, and examined using a Carl Zeiss AXIOVERT 40 MAT optical microscope. The microstructure reveals a dual-phase morphology with elongated ferritic regions aligned along the rolling direction, indicating the strong effect of plastic deformation during cold rolling. In addition, prominent shear bands are visible throughout the microstructure, which reflect intense strain localization.

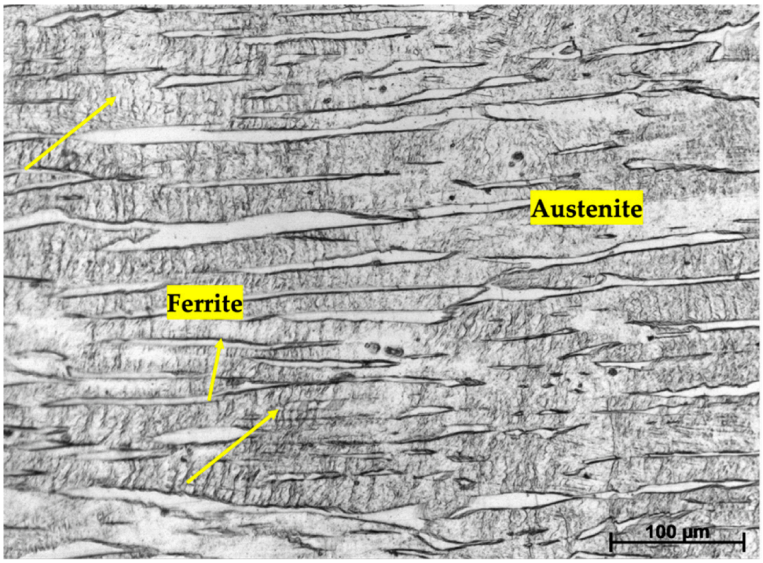


Figure 10. Optical micrograph of the cold-rolled microstructure of a dual phase Fe–22Mn–3Al–3Si–0.01C steel showing shear bands, indicated by yellow arrows.

A detailed TEM investigation of TWIP980 steel [66] revealed a clear evolution of the deformation substructure with increasing strain. In the undeformed condition, the fully recrystallized microstructure contained relatively coarse annealing twins (Figure 11a). Following 10% deformation (Figure 11b), the dislocation density increased markedly and much finer deformation twins, with an average size of nearly 30 nm, began to appear. With increasing deformation (Figure 11c,d), the density of dislocations and deformation twins

progressively increased, particularly at ~40% strain. This enhanced twinning restricted dislocation motion and sustained strain hardening, contributing to the high strength–ductility combination of TWIP steel.

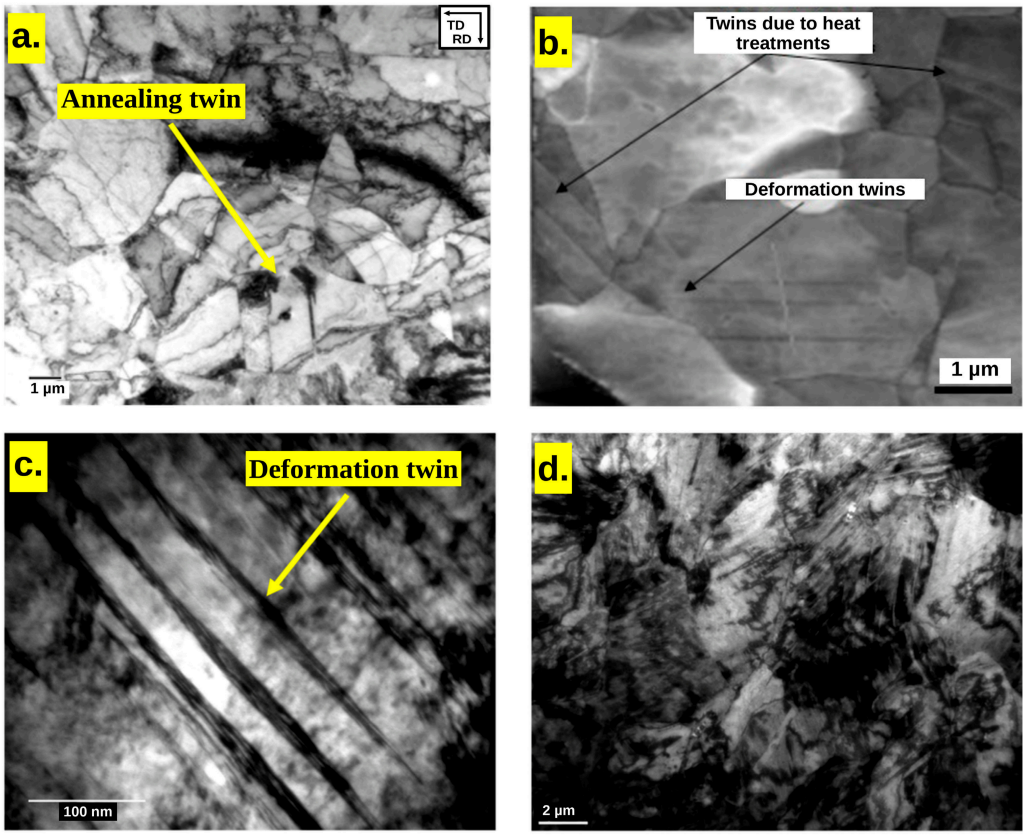


Figure 11. TEM micrographs at different deformation levels: (**a**) undeformed; (**b**) 10% deformation; (**c**) 20% deformation; and (**d**) deformed to a true strain of 40% [66].

4.2.1. Cold Deformation and Evolution of the Deformed Microstructure

Cold rolling introduces large amounts of stored energy into TWIP steels through dislocation multiplication, deformation twinning, stacking-fault formation, shear localization and, in some compositions, deformation-induced phase transformation. With increasing rolling reduction, austenite grains become progressively elongated along the rolling direction while the densities of dislocations and deformation twins increase. In low-carbon Fe–21Mn–3Si–3Al–0.06C steel, deformation twins became progressively more abundant between 10 and 50% cold reduction, and the cold-worked structure contained dislocation substructures, stacking faults and pronounced twin–dislocation interactions. The increase in deformation intensity was accompanied by a marked rise in tensile strength, with the maximum strength appearing after 50% cold deformation, although at the expense of ductility [67].

A similar response was reported for dual-phase Fe–0.07C–20Mn–2.6Si–1.6Al steel, for which 50% cold deformation produced a high density of nanoscale twins and dislocations together with deformation-induced ferrite. The resulting hardness and tensile strength increased to approximately 428 HV and 1419 MPa, respectively. Subsequent annealing at 900 °C reduced the tensile strength to approximately 873 MPa but restored the elongation to about 61%, illustrating the characteristic strengthening–restoration sequence associated with deformation and annealing [68].

Cold deformation can therefore be regarded as the principal strengthening stage of thermomechanical processing. For example, cold rolling to 86% reduction in Fe–18Mn steels containing 0.4 and 0.6 wt.% C generated YS values above 1400 MPa and UTS values above 1600 MPa, although total elongation fell below 30%. Thus, severe cold deformation is highly effective for strengthening TWIP steels, but the accompanying loss of plasticity generally necessitates a subsequent annealing treatment [65].

4.2.2. Recovery and Recrystallization

Upon heating a cold-deformed TWIP steel, the microstructure generally evolves through recovery, partial recrystallization, complete recrystallization and finally grain growth. The temperature ranges associated with these stages depend strongly on composition, amount of prior deformation, precipitation behaviour and heating schedule. During recovery, rearrangement and annihilation of dislocations reduce the stored energy without completely replacing the deformed microstructure. This stage may therefore decrease strength moderately while preserving a significant fraction of deformation twins and substructural barriers. Recrystallization, in contrast, replaces the highly strained microstructure with new defect-poor grains, producing a more pronounced reduction in strength but a substantial restoration of ductility [69].

A Fe–18Mn–0.6C–1.5Al steel was subjected to 20–80% cold rolling followed by 30 min annealing. Recovery dominated at 673 and 773 K, whereas static recrystallization became pronounced at 873 and 973 K. Increasing prior rolling reduction produced smaller recrystallized grains, and grain sizes ranging approximately from 1 to 8 μm could be generated depending on the rolling–annealing condition. Their analysis showed that the final yield strength could be rationalized through the combined contributions of retained dislocation strengthening and grain-size strengthening [70].

The same general sequence was observed in low-carbon Fe–21Mn–3Si–3Al steel. After 10 or 30% cold rolling, annealing between 600 and 800 °C for 5 min predominantly produced recovery, while recrystallization became evident at 900 °C. Increasing cold reduction increased hardness, YS and UTS and reduced elongation; annealing partially reversed this trend by restoring plasticity [71].

The ability to produce ultrafine recrystallized grains is especially salient because it provides a route to increase YS without retaining the very low ductility of a heavily cold-worked condition. Tian et al. demonstrated that repeated cold rolling and annealing of Fe–22Mn–0.6C could generate a fully recrystallized mean grain size as small as approximately 550 nm. A fully recrystallized condition produced YS of 793 MPa, UTS of 1247 MPa and a uniform elongation of 47%, demonstrating that a fine recrystallized structure can retain substantial TWIP-mediated plasticity while achieving considerably higher strength than conventional coarse-grained material [72].

Partially recrystallized structures can provide an alternative strength–ductility strategy. Dini et al. showed that heavily cold-rolled Fe–31Mn–3Al–3Si steel followed by annealing within the partial-recrystallization regime contained a mixture of newly recrystallized submicron grains and strong unrecrystallized regions enriched in nanoscale deformation twins. The unrecrystallized regions preserve deformation-induced strengthening, whereas recrystallized areas contribute to ductility. Consequently, large cold reduction followed by annealing near the lower boundary of the partial-recrystallization regime was proposed as an effective means of obtaining a submicron TWIP steel with a favourable strength–ductility balance [73].

4.2.3. Effect of Grain Size on Mechanical Properties of TWIP Steel

Among the microstructural parameters modified by thermomechanical treatment, austenite grain size has one of the strongest influences on tensile response. Grain refinement increases YS and generally increases UTS through Hall–Petch strengthening, whereas coarser grains tend to favour larger elongation and easier activation of deformation twinning.

Dini et al. studied Fe–31Mn–3Al–3Si with grain sizes from approximately 2.1 to 72.6 μm and showed that grain refinement suppresses deformation twinning because greater stresses are required to generate the dislocation pile-ups needed to initiate twins. Conversely, larger grains facilitate mechanical twinning, and the resulting twin boundaries provide additional instantaneous work hardening that delays necking and increases uniform elongation [74].

This grain-size dependence was quantified for Fe–25Mn–3Cr–3Al–0.3C–0.01N. Increasing the grain size from 2.2 to 28.7 μm reduced YS from approximately 410 to 232.5 MPa and UTS from 725 to 517 MPa, while elongation increased from 15.4 to 54.2%. Deformation twins were also more readily observed as the initial grain size increased. These results exemplify the inherent strength–ductility trade-off arising from grain-size control [75].

Lan and Zhang [76] reported an analogous trend in Fe–22Mn–0.5C steel. Increasing annealing temperature and time promoted recrystallized grain growth and increased the amount and dimensions of annealing twins. As the grain size increased, YS and UTS decreased while total elongation increased. Their data followed Hall–Petch-type behaviour, and a grain-size interval of approximately 10–30 μm was identified as particularly effective for maintaining a strength–ductility product above 65 GPa%. Annealing at 650–750 °C for 15–20 min produced UTS above about 1030 MPa with approximately 60% total elongation, whereas annealing at 850–950 °C for shorter times produced UTS of about 900 MPa together with elongation exceeding 70%.

Grain size also controls the ease of twin nucleation, the available distance for dislocation accumulation and the capacity of the microstructure to generate additional barriers during plastic straining. Hence, an optimum grain size rather than the smallest possible grain size is generally desirable when both high strength and large tensile ductility are required.

4.2.4. Influence of Annealing Temperature and Holding Time

Annealing temperature is typically more influential than moderate changes in holding time because it determines whether recovery, recrystallization, carbide dissolution or grain coarsening dominates. Lan and Zhang [76] found that the most pronounced variation in strength and elongation occurred between approximately 750 and 850 °C, where rapid grain coarsening accompanied complete recrystallization; in their processing range, changing annealing temperature by 100 °C influenced grain size more strongly than changing holding time by 15 min.

Heat-treatment duration nevertheless becomes crucial once the alloy is within a temperature range capable of rapid recovery or recrystallization. In low-carbon dual-phase TWIP steel, annealing at 900 °C progressively reduced the deformation-induced strength and restored ductility as recovery and recrystallization proceeded. The combination of recrystallized and unrecrystallized regions can be especially advantageous at intermediate times because the former accommodates strain while the latter retains high dislocation and twin densities [68].

Tewary et al. investigated this effect systematically in a dual-phase ultrahigh-strength TWIP steel over 500–1000 °C and holding times from 5 min to 2 h. Recovery predominated at approximately 500–600 °C, partial recrystallization developed at 700–800 °C, and near-complete recrystallization occurred around 900 °C and above. Partially recrystallized conditions provided particularly useful property combinations: annealing at 700 °C for 30 min produced UTS of 859 MPa with 37% elongation, whereas 900 °C for 30 min provided

UTS of 708 MPa together with 63% elongation [77]. The corresponding low-carbon dual-phase Fe–0.07C–20Mn–2.6Si–1.6Al study further demonstrated that 50% cold deformation produced the highest strength, whereas annealing at 900 °C reduced residual stresses, dislocation density and fault probability and markedly restored tensile ductility [68]. SEM SEI (secondary electron imaging) fractograph of Fe–22Mn–3Al–3Si–0.1C steel presented in Figure 12, annealed at 700 °C for 10 min reveal predominantly ductile fracture, characterized by dimples associated with microvoid nucleation, growth, and coalescence. The voids refer to cavities within the material, while microvoids are microscopic cavities that develop during plastic deformation. Dimples are the characteristic depressions observed on the fracture surface following microvoid growth and coalescence, indicating ductile fracture.

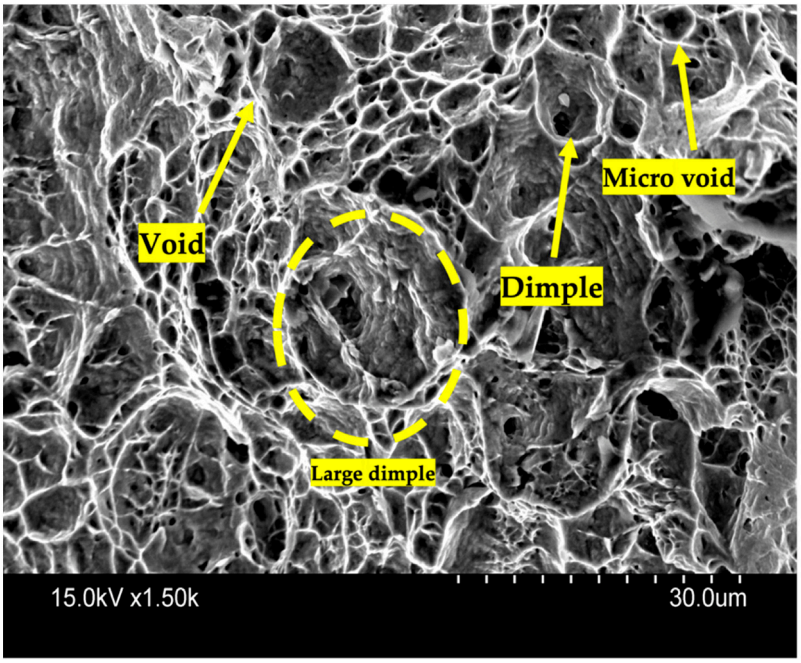


Figure 12. SEM fractograph of Fe–22Mn–3Al–3Si–0.1C steel showing ductile fracture.

4.2.5. Carbide Precipitation and Microalloying Effects

The response to annealing is not governed by recrystallization alone. Carbide precipitation and dissolution can increase strength thereby producing non-monotonic property changes with temperature. Kang et al. reported that recrystallization of 60% cold-rolled Fe–18Mn–0.6C–1.5Al began around 600 °C and was essentially completed at 700 °C after 10 min. Above approximately 840 °C, recrystallized grains coarsened more rapidly. Although strength generally declined and ductility increased with increasing annealing temperature, an anomalous strength increase occurred between 700 and 800 °C because of carbide precipitation hardening [78].

Recent heat-treatment experiments similarly revealed strong interactions between M_3C precipitation and twinning. Annealing at 600–700 °C promoted carbide formation, whereas higher treatments at 800–900 °C reduced the carbide population and allowed twinning to become more prominent. In that study, increasing temperature and holding time generally lowered hardness and tensile strength while increasing elongation [79].

Microalloying provides another route for controlling the competition between recrystallization and strengthening. Schinhammer and group showed that Pd-rich precipitates in cold-worked Fe–Mn–C–Pd alloys delayed recrystallization through both grain-boundary pinning (Zener drag) and solute drag associated with Pd enrichment at dislocation cores.

This delayed restoration allowed a useful combination of high strength, ductility and work-hardening capacity to be retained over suitable processing conditions [80].

Ti microalloying has similarly been used to refine the grain structure and introduce TiC particles. In a low-carbon high-Mn dual-phase TWIP steel, cold deformation increased deformation-induced ferrite and twinning, while annealing at 500, 700 and 900 °C produced recovery, partial recrystallization and near-complete recrystallization, respectively. The 50% cold-deformed condition exhibited YS of about 1176 MPa and UTS of about 1283 MPa, but only around 11% elongation; subsequent annealing at 700 °C increased the ductility, and treatment at 900 °C restored it to approximately 60% [81].

A more recent alloy-design approach combined Al, Si, Mo and V additions with solution treatment, cold rolling and short-time annealing. Solution treatment dissolved coarse precipitates, while subsequent annealing produced fine MC and M_2C particles and refined austenite grains. After solution treatment at 1100 °C for 2 h followed by cold rolling and annealing at 800 °C for 10 min, the steel achieved YS of 877 MPa, UTS of 1457 MPa and elongation of 46.1%. The high strength was attributed primarily to the combined action of grain refinement and nanoscale precipitation strengthening [82].

4.2.6. Stabilization of Deformation Twins by Rapid Heat Treatment

Conventional recrystallization annealing is not the only means of recovering ductility. Ultra-rapid heat treatment can selectively reduce dislocation density while retaining deformation twins introduced by prior cold rolling. Since twins are thermally more stable than many deformation-generated dislocations, such processing can preserve strong barriers to slip while relieving a portion of the cold-worked defect structure.

Fabrègue et al. demonstrated that ultra-rapid heating of cold-rolled high-Mn TWIP steel produced a particularly attractive property balance below the onset of recrystallization. The yield strength remained as high as approximately 1.35 GPa near 615 °C, whereas the appearance of the first recrystallized grains at higher temperature produced a sharp decrease in YS. This behaviour shows that selective recovery while preserving nanoscale deformation twins represents an alternative strategy to conventional full recrystallization when high yield strength is a primary requirement [83].

4.2.7. Phase Constitution, Al Content and Dual-Phase TWIP Steels

Thermomechanical response is also dependent on whether the processed steel remains fully austenitic or contains a ferritic constituent. In low-Al TWIP steels, a duplex austenite–ferrite structure may form, whereas greater Al additions can stabilize a fully austenitic condition. Tewary et al. showed that the lower-Al dual-phase condition exhibited greater hardness and tensile strength but reduced elongation compared with the higher-Al, fully austenitic steel. Following 50% cold reduction, nanoscale deformation twins were evident in both alloys [84].

Deformation-induced ferrite can provide additional strengthening in dual-phase systems. Cold rolling increases both its fraction and the density of deformation twins, while high-temperature annealing may reverse the ferrite toward austenite. Tewary et al. reported that deformation-induced ferrite and twinning contributed to the very high strength of cold-worked material, whereas partial or complete recrystallization and reverse transformation during annealing restored tensile ductility. This behaviour confirms that tensile properties in dual-phase TWIP steels are influenced not only by defect density and grain size but also by the evolving phase fraction during thermomechanical treatment [77].

Figure 13a presents the FESEM microstructure of the Fe–22Mn–3Al–3Si–0.01C dual-phase steel examined using a Merlin FESEM (Carl Zeiss). The alloy was homogenized, cold rolled to 60% thickness reduction, subsequently annealed at 710 °C for 10 min, and water

quenched. The microstructure exhibits elongated ferritic phase regions together with recrystallized austenitic areas containing distinct annealing twins. The occurrence of annealing twins is associated with recrystallization and grain-boundary migration during annealing and is characteristic of FCC austenite with relatively low stacking-fault energy. The accompanying EDS line-scan analysis in Figure 13b further supports the presence of a ferritic phase. Across the elongated phase, a noticeable decrease in Mn concentration is observed together with a comparatively higher Al concentration. Since Mn is an austenite-stabilizing element whereas Al strongly promotes ferrite stability, this compositional partitioning is consistent with the formation of an Al-enriched, Mn-depleted ferritic region adjacent to the austenitic matrix.

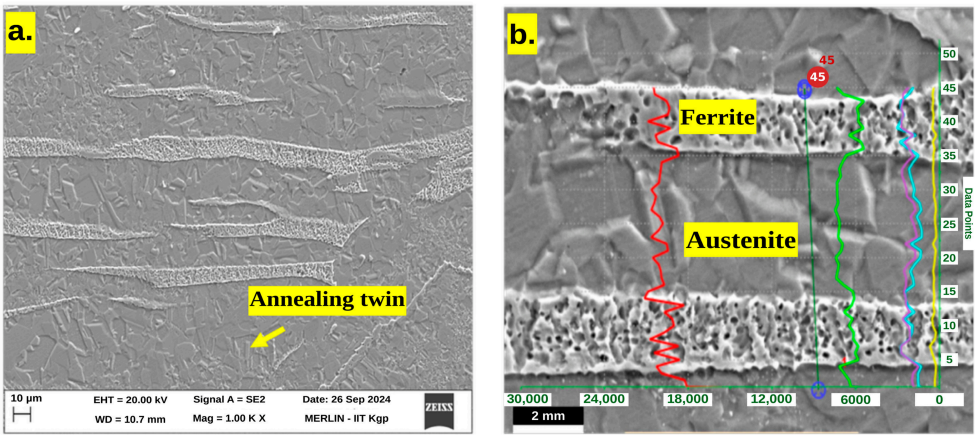


Figure 13. (**a**) FESEM micrograph and (**b**) corresponding EDS line-scan analysis of the annealed Fe–22Mn–3Al–3Si–0.01C steel, showing phase morphology and elemental partitioning, with the red, green, purple, sky blue and yellow profiles representing Fe, Mn, Si, Al and C respectively.

4.3. Hydrogen Embrittlement in TWIP Steels: Mechanisms and Mitigation Strategies

Hydrogen embrittlement (Theme D) has received increasing research attention, with its contribution rising from 2.1% in Phase I to 9.7% in Phase III (Table 4). This growing interest reflects the importance of understanding hydrogen-assisted degradation in TWIP steels. Accordingly, this section critically examines the underlying mechanisms and mitigation strategies.

Hydrogen embrittlement (HE) constitutes one of the major challenges limiting the wider application of high-Mn TWIP steels, particularly in automotive and hydrogen-containing service environments. Although the fully austenitic FCC structure of TWIP steels is generally characterized by relatively low hydrogen diffusivity, hydrogen introduced during processing, corrosion, cathodic charging, or service can accumulate at microstructural defects and highly stressed regions, resulting in premature fracture and severe loss of ductility. A schematic illustration of HE, depicting hydrogen entry, diffusion, accumulation at grain boundaries, and subsequent crack initiation and propagation, is shown in Figure 14. The susceptibility of TWIP steels to hydrogen-assisted failure is therefore governed not merely by the total hydrogen content but by the combined effects of hydrogen trapping, grain and twin boundaries, deformation-induced defects, residual stress, phase stability, stacking fault energy (SFE), and alloy chemistry [85,86].

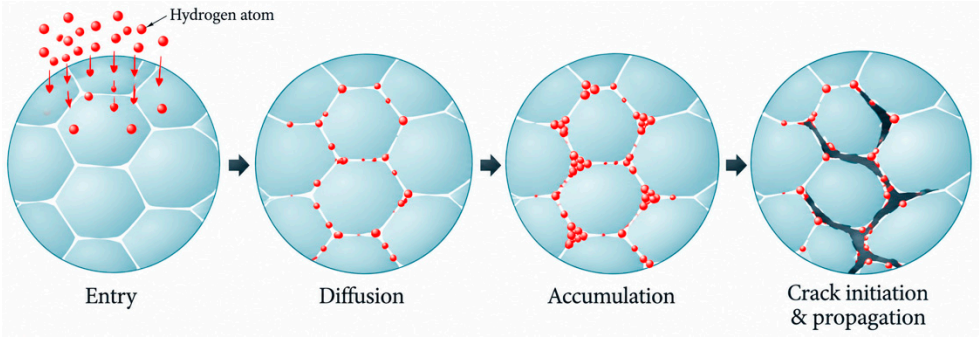


Figure 14. Schematic representation of hydrogen embrittlement.

Early experimental evidence demonstrated that hydrogen can markedly deteriorate the tensile ductility of Fe–Mn–C TWIP steels. In Fe–18Mn–0.6C steel, Koyama et al. reported a reduction in total elongation from approximately 60% to 30% during simultaneous electrochemical hydrogen charging and tensile deformation. The hydrogen-charged specimens exhibited a pronounced intergranular fracture region near the specimen surface, indicating that hydrogen-assisted degradation is closely associated with boundary-controlled fracture rather than a uniform loss of plasticity throughout the material [86]. A subsequent study further demonstrated that tensile deterioration became significant above a critical hydrogen-charging condition and that the fracture stress decreased with increasing diffusible hydrogen content. Interestingly, the work-hardening behaviour remained largely unaffected, suggesting that HE in this alloy was not primarily controlled by changes in conventional slip, twinning, or martensitic transformation, but rather by hydrogen-assisted weakening of susceptible interfaces [87].

The fracture behaviour of TWIP steels under hydrogen exposure is strongly related to grain and twin boundaries. Koyama et al. observed that hydrogen-charged Fe–18Mn–1.2C steel fractured predominantly along grain boundaries, although transgranular cracking was also detected. The transgranular cracks were aligned with primary and secondary deformation-twin boundaries, demonstrating that deformation twins can participate directly in hydrogen-assisted crack initiation and propagation [88]. In situ electron channeling contrast imaging subsequently confirmed that cracks can initiate at both grain boundaries and deformation twins and that crack propagation may proceed along these interfaces. Stress concentration at twin tips was proposed as an important factor promoting hydrogen-assisted cracking [89]. Thus, deformation twinning exhibits a dual role in TWIP steels: while twin boundaries enhance strain hardening by restricting dislocation motion, they may also serve as hydrogen-sensitive interfaces under appropriate loading conditions.

Recent atomic-scale observations provide further support for the role of twin boundaries in HE. Khanchandani et al. employed isotope-labelled atom probe tomography and directly revealed segregation of tritium to coherent twin boundaries in a model TWIP steel. Oxygen was also found to co-segregate at these interfaces. These observations provide direct evidence that twin boundaries can act as preferential sites for hydrogen accumulation and therefore represent potentially vulnerable regions for hydrogen-assisted damage [90].

The interaction of hydrogen with dislocations and stacking faults adds further complexity to the embrittlement mechanism. In situ electrochemical nanoindentation of Fe–22Mn–0.6C steel showed that hydrogen reduced the load required for dislocation nucleation. This behaviour was interpreted through hydrogen-induced reductions in dislocation line energy and stacking fault energy. At the same time, hydrogen increased local nanohardness through changes in lattice resistance and plastic-zone size [91]. These findings are consistent with the view that hydrogen may promote highly localized plasticity while simultaneously increasing the susceptibility of highly stressed interfaces to cracking. Accordingly, HE

in TWIP steels is likely to involve the combined action of hydrogen-enhanced localized plasticity, interfacial decohesion, and defect-assisted hydrogen accumulation rather than a single universal mechanism.

Grain size has been identified as an important microstructural parameter controlling HE susceptibility. Park et al. demonstrated that grain refinement considerably improves the HE resistance of Fe–18Mn–0.6C TWIP steel. Fine-grained specimens exhibited lower densities of deformation twins, twin–twin intersections, and twin–grain-boundary-junctions during deformation, thereby decreasing the number of highly stressed and hydrogen-enriched sites available for crack initiation [92]. This effect is particularly significant in TWIP steels because refinement of the austenite grains increases the stress required for deformation twinning and thus suppresses excessive twin formation. However, the beneficial effect depends on the spatial uniformity of the grain structure. In a bimodal-grained TWIP steel, hydrogen-assisted intergranular cracking was preferentially observed near fine/coarse grain interfaces, whereas coarse-grained regions exhibited transgranular cracking along twin boundaries. The resulting delamination was associated with microvoid nucleation, growth, and coalescence [92].

Among alloying strategies, aluminium has repeatedly been shown to improve the resistance of TWIP steels to hydrogen-assisted delayed fracture. Chun et al. demonstrated that Al-containing TWIP steels possessed substantially greater delayed-fracture resistance than Al-free steel. The improvement was associated with a reduction in diffusible hydrogen-trapping sites, lower residual stress, and favourable deformation texture [93]. Al also increases the SFE and thereby modifies the deformation substructure by reducing intense planar deformation and excessive mechanical-twin localization. Previous work summarized by Park et al. further indicated that an Al-rich oxide layer can form on the steel surface and reduce hydrogen permeation into the material [92]. However, the beneficial effect of Al is sensitive to impurity content; Dieudonné et al. showed that residual phosphorus can substantially reduce the improvement in HE resistance associated with Al addition [94].

Cu alloying has also emerged as an effective strategy for improving HE resistance. Dieudonné et al. reported that Cu and Al additions enhance resistance to intergranular hydrogen-assisted fracture, primarily through an increase in SFE and a corresponding reduction in local stress–strain and hydrogen localization at grain boundaries [94]. More recent work by Dong et al. identified several additional beneficial effects of Cu. Cu addition increased SFE, refined austenite grains after suitable annealing, reduced diffusible hydrogen content through the formation of a Cu-rich surface, and promoted a more dispersed distribution of deformation twins through Cu-rich clusters or precipitates. These combined effects reduced local hydrogen accumulation at vulnerable interfaces and produced a pronounced improvement in HE resistance, particularly in the 700 °C-annealed condition [95].

The influence of silicon is more complex. Lee et al. showed that increasing Si content promotes the formation of an $(Fe,Mn)_2SiO_4$-containing surface oxide that decreases hydrogen permeation. However, despite the lower hydrogen uptake, the loss of elongation increased with increasing Si content, particularly at 3 wt.% Si. In the Si-free and 1.5 wt.% Si steels, hydrogen accumulated preferentially at mechanical twins, whereas in the 3 wt.% Si alloy, ε-martensite formed during deformation and became a dominant hydrogen-enriched region [96]. Therefore, reducing hydrogen ingress alone does not necessarily guarantee improved embrittlement resistance if the alloying addition simultaneously promotes deformation products that serve as efficient hydrogen traps or crack-propagation paths.

The effect of C also requires careful consideration. C is essential for austenite stabilization and solid-solution strengthening in conventional Fe–Mn–C TWIP steels; however, excessive interstitial C may promote hydrogen-sensitive grain-boundary cracking. A comparison between Fe–30Mn–0.6C and Fe–30Mn–3Al–3Si steels showed that the C containing

alloy was more susceptible to HE and exhibited predominantly random grain-boundary cracking. The Al–Si containing steel displayed a mixture of intergranular and transgranular cracking and comparatively better resistance. These results indicate that the role of C should be evaluated together with its influence on austenite stability, boundary chemistry, and deformation behaviour rather than considering it solely as a strengthening or stabilizing element [97].

4.4. Fatigue and Fracture Behaviour of TWIP Steels

In addition to hydrogen embrittlement (Theme D), fatigue behaviour and fracture mechanisms (Theme E) are important considerations in evaluating the service performance and structural reliability of TWIP steels. While hydrogen embrittlement primarily concerns material degradation in hydrogen-containing environments, fatigue and fracture studies focus on the initiation and propagation of cracks under cyclic and dynamic loading conditions. TWIP steels used in automotive structural components are frequently subjected to repeated tensile, compressive, and impact loading during service. Therefore, understanding their fatigue behaviour and fracture mechanisms is essential for evaluating their structural reliability and mechanical performance. Under high-cycle fatigue (HCF) conditions, Hamada et al. [98] investigated three high-Mn TWIP steels with grain sizes ranging from 4.5 to 55 μm. The fatigue limit at 2×10^6 cycles was approximately 400 MPa, corresponding to 42–48% of their tensile strength, which is comparable to that of austenitic stainless steels. During cyclic loading, neither deformation twinning nor ε-martensite formation was observed. Instead, fatigue damage mainly occurred through the formation of intense slip bands, accompanied by surface extrusions and intrusions. Fatigue cracks initiated during the early stages of cycling, within the first 25% of fatigue life, particularly at the intersections of slip bands with grain boundaries and annealing twin boundaries. Crack propagation was predominantly transgranular, with ductile striations observed on the fracture surfaces. The study also demonstrated that grain refinement significantly improved fatigue strength [98]. Further improvements in HCF resistance have been achieved through microstructural modifications and surface treatments. In Fe–30Mn–0.6C steel, a grain-size gradient developed through pre-torsion and subsequent annealing provided better fatigue resistance than homogeneous coarse-grained and fine-grained structures. This improvement was attributed to the formation of geometrically necessary dislocations and a hard-core/soft-shell microstructure, which restricted surface crack initiation [99]. Similarly, surface milling introduced work-hardened layers and compressive residual stresses, resulting in improved fatigue resistance compared with polished surfaces [100]. However, the effect of pre-straining on fatigue behavior is more complex. In TWIP880 steel, compressive pre-straining increased the yield strength and failure stress at 10^4 cycles, whereas the predicted fatigue limit decreased from 306 MPa in the undeformed condition to 225 MPa and 245 MPa after 5% and 10% pre-straining, respectively [101].Under low-cycle fatigue (LCF) conditions, the cyclic deformation behaviour of TWIP steels is strongly influenced by stacking fault energy (SFE). In Fe–22Mn–0.6C steel, the addition of 3 wt.% Al increased the SFE and reduced the planar nature and reversibility of dislocation slip. Consequently, cyclic hardening decreased, cyclic softening increased, and fatigue life was reduced. Deformation twins were observed only in the Al-free steel [102]. In addition to SFE, loading orientation, pre-strain, and testing temperature also affect fatigue performance. In Fe–19Mn–0.4C–1.7Cr–1.2Al steel, testing at 449 K resulted in reduced fatigue life. Unlike the behaviour observed at room temperature, pre-straining significantly decreased fatigue life at elevated temperatures. A fatigue life prediction model incorporating temperature-dependent deformation mechanisms was developed and validated using 77 loading conditions [103]. Similarly, Junak and Jabłońska [104] investigated the LCF behaviour of X60MnAl20-3 TWIP steel under different

loading conditions. The highest fatigue life was observed under compressive strain cycling, whereas tensile strain cycling resulted in the lowest fatigue life. Fracture surface analysis revealed ductile features, including dimples and striations, while deformation twinning became more prominent near the fracture region with increasing strain amplitude.

TWIP steels exhibit different fracture mechanisms depending on loading conditions, specimen geometry, and microstructural characteristics. Luo and Huang [105] reported that fracture in TWIP steels occurred through void-sheet formation or quasi-cleavage cracking, depending on specimen geometry. In contrast, 304 stainless steel and interstitial-free (IF) steel predominantly exhibited void coalescence. The occurrence of quasi-cleavage fracture reduced the notch-strength ratio to approximately 0.7, while the essential work of fracture toughness was approximately 189 kJ/m^2, which is considerably lower than that of 304 stainless steel [105]. Under dynamic loading at strain rates ranging from 700 to 3000 s^{-1}, the adiabatic temperature increased by approximately 110 K, raising the SFE above 50 mJ/m^2 and suppressing deformation twinning. The accumulation of dislocations at grain and twin boundaries promoted localised deformation and microcrack initiation. Consequently, the fracture mode changed from ductile fracture, characterised by dimples, to quasi-cleavage fracture with river patterns [106]. Fracture behaviour during wire drawing was investigated in another study, which reported that cracks initiated in the near-surface region rather than directly at the surface. This region exhibited higher effective and shear strains, greater twinning activity, and increased geometrically necessary dislocation density, along with relatively lower temperatures. Increasing the reduction per pass improved drawability by increasing the deformation temperature and consequently the SFE [107]. Alloying elements also influence fracture toughness. In Fe–22Mn–0.6C steel, J-integral testing revealed provisional fracture toughness (JQ) values of 764.3 and 892.2 kJ/m^2 for steels containing 0 and 5 wt.% Cr, respectively. However, increasing the Cr content to 10 wt.% significantly reduced the valid fracture toughness (JIC) to 79.2 kJ/m^2. This reduction was attributed to the formation of segregation bands and chromium carbides along grain boundaries, which promoted intergranular fracture [108].

5. Application of Machine Learning in TWIP Steels

The previous sections have discussed the fundamental deformation mechanisms, microstructural evolution, and mechanical behaviour of TWIP steels, along with their performance under different service conditions. Understanding the complex relationships among these factors is essential for predicting material behaviour and developing TWIP steels with improved mechanical performance. In this context, ML and data-driven design (Theme F) have gained increasing research interest, although they represent the least explored theme in the bibliometric dataset (Table 4). After an early ANN study in 2009 [10], research activity in this theme resumed only from 2022 onwards.

The mechanical response of TWIP steels is governed by strongly coupled relationships among chemical composition, SFEs, thermomechanical processing, grain size, deformation substructure and testing conditions [1]. Conventional experimental approaches generally investigate these variables individually or through a restricted number of alloy/process combinations, making exploration of the large multidimensional design space time- and resource-intensive. ML has therefore emerged as a useful complementary approach for identifying nonlinear composition–microstructure–property relationships, predicting mechanical behaviour, analysing microstructural evolution and, more recently, assisting the inverse design and fatigue assessment of TWIP steels [109]. A schematic illustration of the evolution of ML applications in TWIP steels, progressing from early ANN-based property prediction to microstructure-informed learning, interpretable inverse design, auto-

mated microscopy, fatigue-property prediction, and whole-life cyclic modelling, is shown in Figure 15.

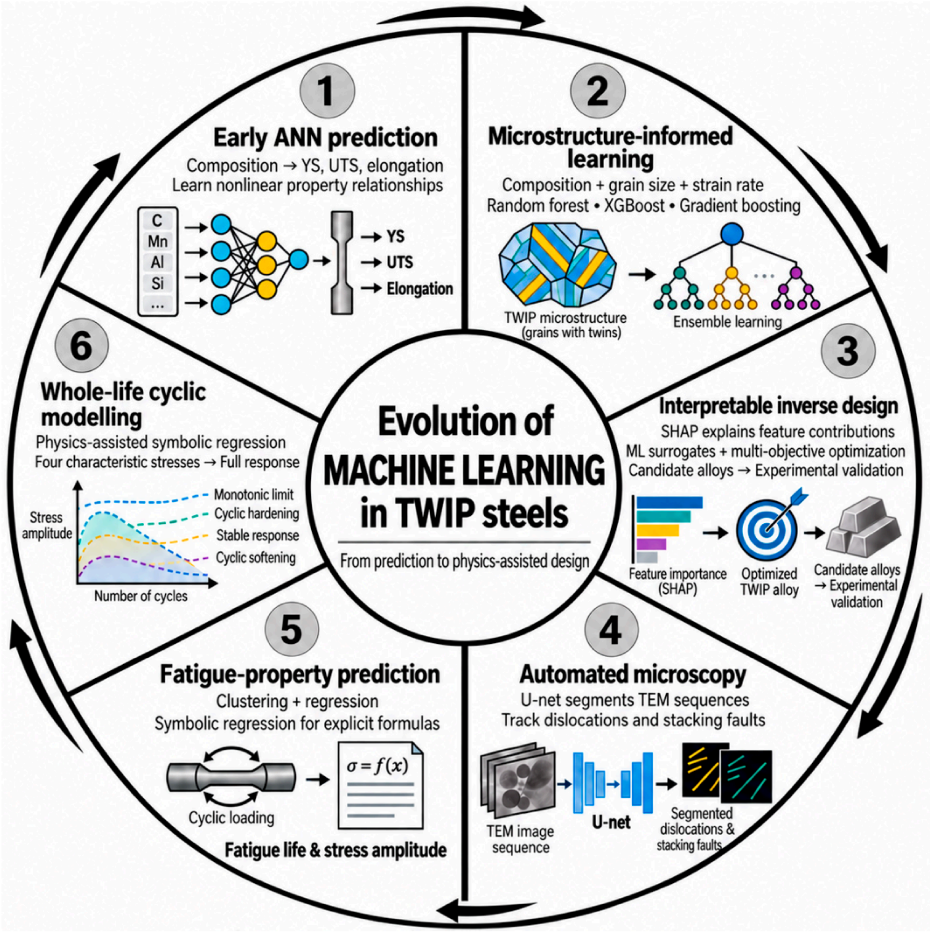


Figure 15. Schematic representation of the evolution of application of machine learning in TWIP steel.

5.1. Machine Learning for Mechanical-Property Prediction

One of the earliest applications of ML to high-Mn TRIP/TWIP steels was reported by Dini et al., who developed an artificial neural network (ANN) to predict yield strength, ultimate tensile strength and total elongation as functions of Mn, Si and Al contents. The investigated compositional ranges were 15–30 wt.% Mn and 2–4 wt.% each of Si and Al, and the ANN predictions showed good agreement with experimental data. The model employed a feed-forward architecture with two hidden layers, with the final network containing six neurons in the first hidden layer and four in the second, thereby establishing a 3–6–4–3 architecture. The ANN analysis also provided useful compositional trends. Increasing Mn content was predicted to decrease YS and UTS while generally increasing elongation, whereas changes in the Si/Al ratio modified both strength and ductility. These results reflected the transition between TRIP- and TWIP-dominated deformation regimes and demonstrated that ML could be used not only for numerical prediction but also for exploring composition–property trends within an experimentally established domain. However, the model incorporated composition alone and therefore did not explicitly describe the important effects of grain size and thermomechanical history on the final mechanical response [10].

Subsequent studies have progressively introduced microstructural descriptors into ML frameworks. In the regression study by Sinha et al., composition and grain size were employed for predicting the yield strength of TWIP steel using several regression algorithms.

Random forest regression provided the highest predictive accuracy, with $R^2 \approx 0.80$ and the lowest mean-square error among the models considered. This represents an important development beyond composition-only modelling because grain size carries information regarding thermomechanical processing and Hall–Petch strengthening. The result also illustrates the suitability of tree-based ensemble approaches for TWIP-steel datasets, where the relationships between composition, microstructure and mechanical properties are strongly nonlinear and may involve complex feature interactions [110].

A more comprehensive data-driven strategy was subsequently developed by Zhou et al. for the design of high-yield-strength TWIP steels. Their database contained 273 literature-derived observations incorporating alloy composition, grain size, tensile-test strain rate and corresponding YS, UTS and elongation. The study compared linear regression, support vector regression, ANN, XGBoost, gradient boosting regression and random forest regression. Ensemble algorithms were found to provide particularly effective prediction of the complex mechanical response; XGBoost produced the lowest mean absolute percentage errors for YS and UTS, approximately 8.47% and 4.88%, respectively, while gradient boosting regression gave the best elongation prediction with a MAPE of approximately 10.04% [111].

This work marked an important shift from forward prediction toward data-driven alloy design. Rather than using ML only to estimate properties for a specified composition, SHapley Additive exPlanations (SHAP) were applied to quantify the effects of individual composition and microstructural variables on YS, UTS and elongation. The resulting surrogate models were subsequently coupled with multi-objective optimization to identify compositions capable of simultaneously increasing yield strength and retaining a high strength–ductility product. Experimental verification of two ML-designed compositions yielded YS values of 585 and 560 MPa, UTS values of 1055 and 1101 MPa and elongations of 55 and 58.5%, respectively. Thus, the study demonstrated the potential of ML to transition from descriptive prediction to an integrated composition–microstructure–property design framework [111].

An important feature of this approach was the treatment of processing information. Because literature-derived processing routes were highly heterogeneous and often incompletely reported, Zhou et al. [111] used final recrystallized grain size as a microstructural descriptor instead of directly encoding numerous forging, rolling and annealing variables. The strategy reduced input dimensionality and missing-data problems, but it also highlights an unresolved limitation of current TWIP-steel ML models: grain size alone cannot fully represent processing-induced differences in dislocation density, annealing-twin density, deformation-twin fraction, precipitation state, texture, residual stress or SFE. Hence, future models would benefit from explicit integration of thermomechanical variables together with physically meaningful microstructural descriptors.

5.2. Machine Learning for Microstructural and Deformation-Mechanism Analysis

The application of ML in TWIP steels has recently extended beyond scalar mechanical-property prediction toward automated characterization of deformation mechanisms. This development is particularly relevant because the TWIP response originates from the continuous evolution of dislocations, stacking faults and mechanical twins, which are conventionally quantified manually from microscopy images.

Tanaka et al. employed a U-net-based semantic-segmentation framework for the quantitative analysis of in situ TEM videos of Fe–22Mn–0.6C TWIP steel. The model distinguished dislocations, stacking faults and background regions, allowing continuous defect evolution to be quantified with the temporal resolution of the original TEM recordings. Specimens with average grain sizes of 0.86, 2 and 8.4 μm were examined, enabling the relationship between grain size and active plasticity carrier to be assessed directly [112].

The importance of this approach lies in replacing isolated, manually selected TEM observations with quantitative time-resolved defect measurements. In the ultrafine-grained 0.86 μm specimen, a rapid increase in stacking-fault fraction was observed near macroscopic yielding, whereas the relative contributions of stacking faults and dislocations differed in the coarser-grained specimens. The rapid stacking-fault increase was closely associated with discontinuous yielding, suggesting that the release of stored elastic energy through rapid fault generation contributes to the macroscopic yield event [112]. Hence, ML-based image analysis provides an important bridge between microscopic defect kinetics and macroscopic mechanical response, a capability that conventional regression models based solely on tabular composition/property data cannot provide.

5.3. Machine Learning for Fatigue-Property Prediction

A further development is the use of ML for cyclic deformation and fatigue, where TWIP steels present particular modelling difficulties because the dominant deformation mechanism depends on temperature, pre-strain, texture, loading direction and strain amplitude. Wu et al. developed both black-box and white-box ML models for simultaneous prediction of fatigue life and maximum stress amplitude in Fe–Mn–C–Cr–Al TWIP steel under different loading conditions. Their experimental variables included preloading condition, temperature, strain amplitude, mean strain and loading orientation [113].

The black-box framework combined dimensionality reduction, clustering and regression, thereby allowing samples exhibiting similar fatigue behaviour to be grouped before property prediction. The model achieved fatigue-life predictions entirely within a threefold error band and 88.31% within a twofold band, while all predicted maximum stress amplitudes remained within a 1.51-fold error band. In parallel, symbolic regression was employed as a white-box strategy to derive explicit predictive formulas rather than relying exclusively on opaque numerical mappings. The best symbolic expressions provided 98% of fatigue-life predictions within a twofold error band and all maximum-stress-amplitude predictions within a 1.09-fold band [113].

This comparison between black-box and white-box approaches is particularly relevant to materials design. Ensemble models and neural networks can provide high predictive accuracy but often offer limited direct physical interpretation, whereas symbolic regression can generate explicit mathematical relationships that are easier to examine against known deformation physics. Accordingly, combining both approaches may be advantageous for TWIP steels, where prediction accuracy must eventually be reconciled with established knowledge concerning SFEs, twinning, dislocation slip and temperature-dependent deformation.

The fatigue dataset employed by Wu et al. consisted of 77 valid experimental conditions characterized by loading angle, strain amplitude, maximum strain, mean strain and temperature, with fatigue life and maximum stress amplitude as the two outputs. This multivariable framework is significant because it moves beyond single-property predictions and recognizes that component design requires simultaneous assessment of several service-related responses.

5.4. Prediction of Whole-Life Cyclic Behaviour

More recent work has extended ML from fatigue-life prediction to prediction of the complete evolution of stress amplitude throughout cyclic loading. Song and group combined a physically motivated fatigue-failure framework with symbolic-regression-based ML for high-Mn TWIP steel subjected to variations in loading orientation, pre-strain, temperature and strain amplitude. Rather than attempting to fit every cycle independently, the framework first predicted four representative stress amplitudes corresponding to the initial cycle,

maximum stress, half-life and failure. These characteristic values were subsequently used to reconstruct the entire cyclic stress-amplitude evolution [114].

The resulting fatigue-life prediction showed 96.1% of values within a twofold error band, while 96.4% of the characteristic stress-amplitude predictions were within a 1.2-fold band. The symbolic-regression model subsequently reconstructed the full evolution curve with 99.7% of the data lying within a 1.2-fold error band, an overall R^2 of 0.95 and a MAPE of 1.87%. This approach illustrates an important future direction for ML in TWIP steels: prediction of time- or cycle-dependent material behaviour, rather than prediction of only a final scalar property [114].

6. Scientific Trends and Research Perspectives Emerging from the Bibliometric Analysis

The bibliometric findings provide an overview of the scientific evolution of TWIP-steel research and help establish a connection between publication trends and the major scientific developments discussed in the preceding sections. The annual publication trends (Figure 3) indicate that TWIP-steel research experienced substantial growth during Phase II (2012–2018), followed by a comparatively moderate publication output during Phase III (2019–2026). The country-level collaboration and citation analyses (Figures 4 and 5) further demonstrate the international nature of this research domain, with China, South Korea, and Germany emerging as major contributors. The highly cited publications presented in Table 3 predominantly focus on stacking-fault energy, deformation twinning, dislocation interactions, grain-size effects, and strain-hardening behaviour. These findings indicate that understanding the fundamental deformation mechanisms and microstructure–property relationships has remained central to TWIP-steel research.

The evolution of the research themes presented in Table 4 further reveals changes in scientific priorities. Although fundamental deformation mechanisms (Theme A) remain a major research area, their relative contribution has gradually declined over the successive research phases. In contrast, thermomechanical processing and microstructural development (Theme B) have received increasing research attention. These trends are consistent with the scientific developments reviewed in Sections 4.1 and 4.2, which discuss the influence of stacking-fault energy, deformation twinning, alloy chemistry, and processing conditions on microstructural evolution and mechanical properties. Similarly, the growing research interest in hydrogen embrittlement (Theme D), fatigue, and fracture behaviour (Theme E) indicates increasing attention towards the service performance and structural reliability of TWIP steels, as discussed in Sections 4.3 and 4.4.

In comparison, ML and data-driven design (Theme F) remain relatively underexplored. Nevertheless, the recent emergence of studies involving ML for mechanical property prediction and alloy optimisation, as reviewed in Section 5, indicates the potential for integrating computational approaches with established metallurgical knowledge. Altogether, the bibliometric findings and critical literature review suggest a gradual broadening of TWIP-steel research from fundamental deformation mechanisms towards processing optimisation, service-related performance, and data-driven materials development. However, the continued importance of microstructure–property relationships indicate that future advances will require better integration of alloy design, processing conditions, deformation mechanisms, and mechanical performance.

7. Research Gaps and Future Directions: What Do We Really Need to Do to Unlock the Full Potential of TWIP Steels?

The development of high-Mn TWIP steels was initially accompanied by a rapid increase in scientific activity because of their unusual ability to combine very high tensile strength with exceptional ductility and strain-hardening capacity. Classical investigations established the fundamental roles of SFE, dislocation glide, deformation twinning, grain size, texture, dynamic strain ageing, and thermomechanical processing in governing their mechanical response. However, the annual publication output presented in Figure 3 indicates that TWIP-steel research has gradually transitioned from a period of rapid expansion to a comparatively mature and fluctuating phase. This change should not necessarily be interpreted as a reduction in the scientific relevance of TWIP steels; instead, it appears to coincide with a set of persistent technological barriers that have restricted their large-scale industrial penetration and redirected substantial research effort toward alternative third-generation advanced high-strength steels. Despite these challenges, industrial developments such as POSCO's 950TWIP grade, ArcelorMittal's X-IP^{TM}1000, and thyssenkrupp Steel's X40MnCrAlV19-2 variants consisting of high yield strength (550–750) and low yield strength (300–450), demonstrate the technological feasibility of TWIP steels, although their commercial adoption remains limited compared with conventional AHSS. Figure 16 summarizes the major research gaps presently limiting the broader development of TWIP steels and highlights corresponding future directions. In line with the themes of Table 4 and the synthesis in Section 6, the gaps below are discussed in the order of the remaining barriers: lean alloy design and processing (Theme C), service performance (Themes D and E) and data-driven design (Theme F).

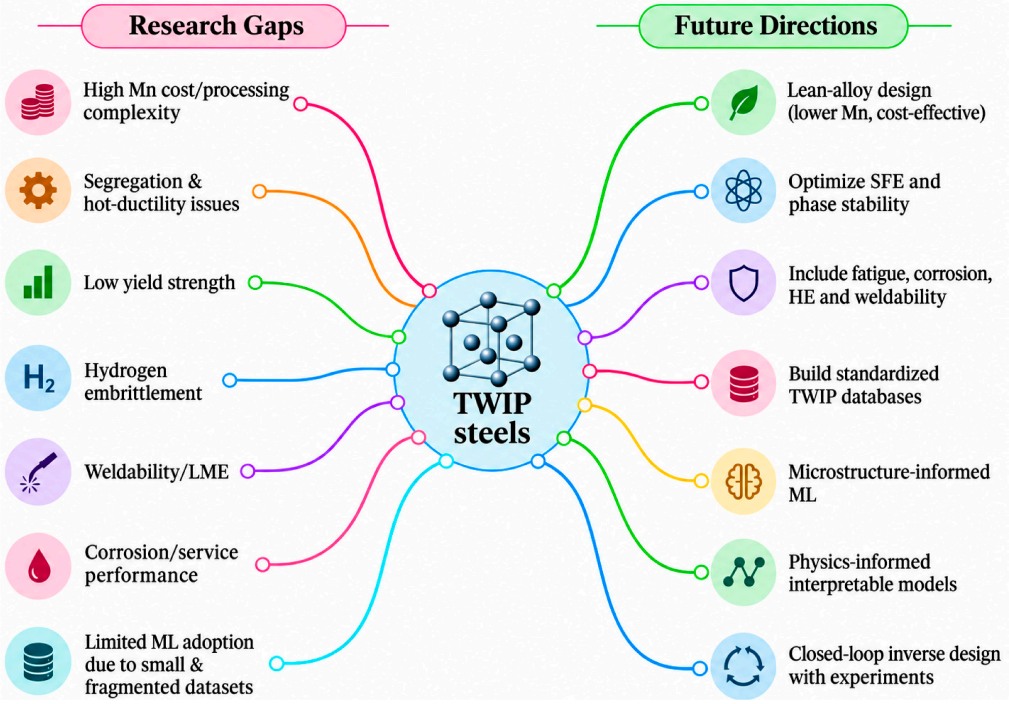


Figure 16. Schematic representation of the major research gaps and future directions in TWIP steels.

One of the principal limitations remains the high Mn content required to stabilize the austenitic matrix and maintain an appropriate SFE for twinning. Conventional TWIP grades frequently contain approximately 15–30 wt.% Mn [1], which increases alloying cost and introduces difficulties during steelmaking, casting, homogenization, hot processing, and continuous production [89,115]. High-Mn steels are particularly susceptible to chemical

segregation during solidification, while their alloy chemistry can complicate mould-flux behaviour, hot ductility, and surface quality [116]. The combination of expensive alloying additions and increased processing complexity therefore reduces their competitiveness against leaner AHSS.

This shift is particularly evident in the growing attention directed toward medium-Mn third-generation AHSS, which can develop multiphase microstructures containing retained austenite and exploit both TWIP and TRIP mechanisms. Kwok and Dye emphasized that medium-Mn steels have attracted considerable interest because they offer high strength and ductility at lower cost than their high-Mn TWIP predecessors [117]. Thus, part of the apparent moderation in TWIP-steel publication growth can reasonably be associated with a diversification of the research landscape rather than complete abandonment of twinning-assisted alloy design. Future TWIP research should therefore be translated beyond the conventional concept of simply increasing Mn content and instead focussing on lean-alloy strategies in which C, Mn, Al, Si and microalloying additions are jointly optimized to achieve the desired phase stability and SFE with minimum alloying burden.

The engineering implementation of TWIP steels is also constrained by properties that are not adequately represented by conventional tensile testing. HE and delayed fracture remain particularly important because hydrogen interacts strongly with dislocations, stacking faults, deformation twins, and grain boundaries. High-Mn TWIP steels can exhibit hydrogen-assisted intergranular fracture, and aluminium additions have been reported to reduce susceptibility, although the underlying mechanisms remain complex [93]. More recent work further demonstrates that dislocation density and deformation-generated substructures can significantly modify hydrogen uptake and hydrogen-assisted cracking. Consequently, future alloy development should treat hydrogen resistance as a design objective. This requires simultaneous optimization of SFE, grain-boundary character, dislocation density, twin morphology, phase stability, hydrogen trapping behaviour, residual stress and protective surface treatments.

A further industrial limitation is the susceptibility of Zn-coated TWIP sheets to liquid-metal embrittlement (LME) during resistance spot welding. Earlier studies demonstrated that liquid Zn can penetrate susceptible grain boundaries during welding and initiate severe cracking, while recent work continues to investigate stress-assisted grain-boundary Zn diffusion as an important mechanism controlling LME [118]. The persistence of this problem even in recent investigations indicates that weldability remains a practical barrier rather than a completely resolved issue. Future studies should therefore establish the effects of welding parameters, coating characteristics, grain-boundary properties, and local stress conditions on LME susceptibility, while developing effective strategies to minimise Zn penetration and crack formation.

Corrosion behaviour represents another comparatively underdeveloped aspect. Bastidas et al. showed that corrosion performance depends strongly on composition, processing, phase segregation, grain structure and environmental conditions, with pitting, galvanic corrosion, stress-corrosion cracking and hydrogen-related degradation all requiring further attention [3]. The continued emphasis of much of the TWIP literature on monotonic tensile properties therefore provides only a partial description of service performance. Future development should increasingly incorporate fatigue resistance, corrosion, hydrogen-assisted degradation, fracture toughness, weldability, crashworthiness and cyclic loading into alloy and process optimization. TWIP steels are unlikely to achieve wider application simply by demonstrating another increment in UTS or elongation; the more important challenge is to demonstrate reliable performance throughout manufacture and service.

An especially significant research gap is the limited penetration of ML into TWIP-steel design compared with the complexity of the underlying materials problem. TWIP steels

are particularly suitable for data-driven approaches because their behaviour emerges from a highly nonlinear hierarchy. Relatively few studies have attempted to model the entire processing–structure–property relationship using modern ML methods.

The comparatively slow adoption of ML cannot, however, be attributed simply to a lack of algorithms. The more fundamental limitation is the scarcity and fragmentation of high-quality TWIP-specific datasets. Even recent ML studies rely on databases containing only a few hundred observations; the high-yield-strength design work of Zhou et al., for example, employed 273 entries [111]. Such datasets are small relative to the dimensionality of the problem.

A second methodological concern is model validation. The literature datasets frequently contain several observations produced from the same alloy or publication under slightly different processing conditions. Randomly dividing individual rows into training and testing subsets can therefore allow closely related specimens to occur on both sides of the split, producing an optimistic estimate of generalization. Future work should increasingly adopt study-wise, alloy-wise or composition-wise hold-out strategies, followed wherever possible by independent experimental validation. The most convincing demonstration of ML-enabled materials design is not prediction of the previously measured literature data but successful fabrication of an alloy or processing condition that was absent from the training database.

The next step should therefore be a shift from conventional black-box property prediction toward physics-informed and interpretable materials intelligence. Thermodynamic calculations of phase stability and SFEs can provide physically meaningful descriptors; CALPHAD predictions can constrain feasible phase regions; microscopy and diffraction can provide microstructural descriptors; and ML can then learn the remaining nonlinear interactions. Explainability approaches such as SHAP are useful for identifying influential variables, but their interpretations should be assessed against established metallurgy rather than treated as causal evidence by themselves. Multi-objective algorithms can subsequently search the composition–processing space while simultaneously considering YS, UTS, elongation, cost, density, hydrogen resistance, corrosion behaviour and processing feasibility.

Automated characterization provides another major opportunity. The demonstration by Tanaka et al. [112] that dislocations and stacking faults can be extracted automatically from TEM videos indicates that future databases need not remain restricted to manually tabulated scalar parameters. Deep-learning-based segmentation of optical, SEM, EBSD and TEM data could permit systematic quantification of grain size, twin fraction, twin spacing, phase distribution, shear bands and defect density. Integrating such image-derived descriptors with composition and processing variables would establish a genuinely microstructure-informed ML framework, thereby reducing the current disconnect between metallurgical mechanism studies and data-driven property prediction.

Ultimately, the future of TWIP-steel research may depend less on discovering another isolated composition and more on establishing a closed-loop materials-design framework. Such a framework would begin with physics- and literature-informed databases, usage of ML to predict properties and quantify uncertainty, employ multi-objective optimization to propose new compositions and thermomechanical routes, experimentally manufacture and characterize the most informative candidates, and feed those results back into the database. In this manner, ML would not replace physical metallurgy but would provide a mechanism for navigating an experimental design space that is too large to explore systematically by trial and error.

The reduced growth rate observed in the recent TWIP-steel literature should therefore be viewed as an indication that the field has reached a stage where incremental

composition–property studies alone may no longer be sufficient. High alloying cost, processing difficulties, relatively low yield strength, hydrogen embrittlement, corrosion, LME and competition from medium-Mn and other third-generation AHSS continue to restrict widespread implementation. At the same time, the limited availability of standardized, mechanism-rich datasets has prevented TWIP steels from benefiting fully from the rapid advances occurring in materials informatics. Addressing these two problems together offers a promising route for revitalizing the field. Future TWIP research should consequently evolve from isolated experimental optimization toward an integrated composition–processing–microstructure–mechanism–property design philosophy, supported by interpretable ML, uncertainty quantification, multi-objective inverse design and rigorous experimental validation. Such an approach could transform TWIP-steel development from predominantly retrospective understanding into predictive and application-oriented materials design.

8. Concluding Remarks

TWIP steels continue to represent an important class of advanced high-strength steels because of their exceptional strength–ductility synergy and sustained strain-hardening capability. The present bibliometric and critical review demonstrates that the field has developed from fundamental investigations of stacking-fault energy, deformation twinning, dislocation activity, and alloy chemistry toward increasingly complex studies involving thermomechanical processing, service-related behaviour, and data-driven materials design. The bibliometric assessment further indicates that, after a period of rapid expansion, TWIP-steel research has entered a comparatively mature and fluctuating stage, suggesting the need for a shift from incremental investigations toward more integrated and application-oriented research. The analysis of research phases and the evolution of major research themes reveals a gradual shift in research priorities despite the decline in publication output since 2018. From Phase I to Phase III, the proportion of publications focusing on hydrogen embrittlement increased from 2.1% to 9.7%, while studies related to fatigue behaviour and fracture mechanisms increased from 10.8% to 21.6%. In contrast, the contribution of research focusing on fundamental deformation mechanisms showed a slight decline, although these studies continued to dominate the highly cited publications. Meanwhile, ML and data-driven approaches accounted for only 0.5% of the total publications, indicating that their application in TWIP steel research remains relatively limited. These findings suggest a gradual transition in research interest from fundamental deformation mechanisms towards service-related performance and emerging computational approaches.

Although substantial progress has been achieved in understanding the composition, processing, microstructure and property relationships of TWIP steels, several scientific and technological challenges continue to restrict their broader implementation. Future research should therefore emphasize coordinated alloy and process design, improved service-performance assessment, and stronger integration of experimental metallurgy with computational and data-driven approaches. In particular, the comparatively limited adoption of ML remains a salient opportunity, but its effective implementation will require larger, standardized, and mechanism-rich datasets together with robust validation strategies.

The future development of TWIP steels should consequently progress toward an integrated composition, processing, microstructure, mechanism and property framework, supported by physics-informed ML, interpretable modelling, multi-objective optimization, automated characterization, and rigorous experimental validation. Such a transition from isolated empirical optimization toward predictive and closed-loop materials design could accelerate the development of more economical, reliable, and application-

ready TWIP steels and help translate their established scientific advantages into broader engineering utilization.

Author Contributions: Conceptualization, S.S. and M.G.; methodology, S.S.; software, S.S. and P.D.; formal analysis, S.S. and A.G.; investigation, S.S.; data curation, S.S. and P.D.; writing—original draft preparation, S.S.; writing—review and editing, A.B.M., A.G. and M.G.; visualization, S.S. and P.D.; and supervision, A.B.M. and M.G. All authors have read and agreed to the published version of the manuscript.

Funding: This research received no external funding.

Data Availability Statement: The original contributions presented in this study are included in the article. Further inquiries can be directed to the corresponding author.

Acknowledgments: The first author Samjukta Sinha gratefully acknowledges the DST INSPIRE program, Department of Science and Technology, Government of India, for financial support. During the preparation of this manuscript, the authors used GPT-6 Astra and GPT Image 2 (Open AI), for the purposes of generating the graphical icons. The authors have reviewed and edited the output and take full responsibility for the content of this publication.

Conflicts of Interest: The authors declare no conflicts of interest.

References

1. De Cooman, B.C.; Kwon, O.; Chin, K.-G. State-of-the-knowledge on TWIP steel. *Mater. Sci. Technol.* **2012**, *28*, 513–527. [CrossRef]
2. De Moor, E.; Gibbs, P.J.; Speer, J.G.; Matlock, D.K.; Schroth, J.G. Strategies for third-generation advanced high-strength steel development. *AIST Trans.* **2010**, *7*, 133–144.
3. Bastidas, D.M.; Ress, J.; Bosch, J.; Martin, U. Corrosion mechanisms of high-Mn twinning-induced plasticity (TWIP) steels: A critical review. *Metals* **2021**, *11*, 287. [CrossRef]
4. Alza, V.A. TWIP steels: Mechanical and metallurgical properties—A review. *J. Multidiscip. Eng. Sci. Technol.* **2021**, *8*, 1–17.
5. Khosravifard, A.; Hamada, A.S.; Moshksar, M.M.; Ebrahimi, R.; Porter, D.A.; Karjalainen, L.P. High temperature deformation behavior of two as-cast high-manganese TWIP steels. *Mater. Sci. Eng. A* **2013**, *582*, 15–21. [CrossRef]
6. Cornette, D.; Cugy, P.; Hildenbrand, A.; Bouzekri, M.; Lovato, G. Ultra high strength FeMn TWIP steels for automotive safety parts. *Rev. Métall.* **2005**, *102*, 905–918. [CrossRef]
7. Grässel, O.; Krüger, L.; Frommeyer, G.; Meyer, L.W. High strength Fe–Mn–(Al, Si) TRIP/TWIP steels development–properties–application. *Int. J. Plast.* **2000**, *16*, 1391–1409. [CrossRef]
8. Hamada, A.S.; Karjalainen, L.P. Hot ductility behaviour of high-Mn TWIP steels. *Mater. Sci. Eng. A* **2011**, *528*, 1819–1827. [CrossRef]
9. Ohring, M. *Engineering Materials Science*; Academic Press: San Diego, CA, USA, 1995.
10. Dini, G.; Najafizadeh, A.; Monir-Vaghefi, S.M.; Ebnonnasir, A. Predicting of mechanical properties of Fe–Mn–(Al, Si) TRIP/TWIP steels using neural network modeling. *Comput. Mater. Sci.* **2009**, *45*, 959–965. [CrossRef]
11. Tewary, N.K.; Ghosh, S.K.; Bera, S.; Chakrabarti, D.; Chatterjee, S. Influence of cold rolling on microstructure, texture and mechanical properties of low carbon high Mn TWIP steel. *Mater. Sci. Eng. A* **2014**, *615*, 405–415. [CrossRef]
12. Wang, X.J.; Sun, X.J.; Song, C.; Chen, H.; Han, W.; Pan, F. Enhancement of yield strength by chromium/nitrogen alloying in high-manganese cryogenic steel. *Mater. Sci. Eng. A* **2017**, *698*, 110–116. [CrossRef]
13. Zhong, L.; Wang, Z.; Luo, Q.; Liu, W. Effects of cerium addition on the microstructure, mechanical properties and strain hardening behavior of TWIP steel Fe-18Mn-0.6C. *Mater. Charact.* **2022**, *183*, 111626. [CrossRef]
14. WorldAutoSteel. AHSS Insights Blog: A New Global Formability Diagram. World Steel Association. 2021. Available online: https://ahssinsights.org/blog/a-new-global-formability-diagram/ (accessed on 21 August 2026).
15. Feng, X.; Liu, X.; Bai, S.; Ye, Y.; Zong, L.; Tang, Y. Mechanical properties and deformation behaviour of TWIP steel at different strain rates. *Mater. Sci. Eng. A* **2023**, *879*, 145182. [CrossRef]
16. Kim, J.-K.; Kwon, M.-H.; De Cooman, B.C. On the deformation twinning mechanisms in twinning-induced plasticity steel. *Acta Mater.* **2017**, *141*, 444–455. [CrossRef]
17. Zupic, I.; Čater, T. Bibliometric methods in management and organization. *Organ. Res. Methods* **2015**, *18*, 429–472. [CrossRef]
18. Van Eck, N.J.; Waltman, L. Visualizing bibliometric networks. In *Measuring Scholarly Impact: Methods and Practice*; Springer: Berlin/Heidelberg, Germany, 2014; pp. 285–320.

19. Ahmad, T.; Murad, M.A.; Baig, M.; Hui, J. Research trends in COVID-19 vaccine: A bibliometric analysis. *Hum. Vaccines Immunother.* **2021**, *17*, 2367–2372. [CrossRef]
20. Kar, S.K.; Harichandan, S.; Roy, B. Bibliometric analysis of the research on hydrogen economy: An analysis of current findings and roadmap ahead. *Int. J. Hydrogen Energy* **2022**, *47*, 10803–10824. [CrossRef]
21. Rong, H.; Duan, Y.; Zhang, G. A bibliometric analysis of membrane computing (1998–2019). *J. Membr. Comput.* **2022**, *4*, 177–207. [CrossRef]
22. Khudzari, J., Md; Kurian, J.; Tartakovsky, B.; Raghavan, G.V. Bibliometric analysis of global research trends on microbial fuel cells using Scopus database. *Biochem. Eng. J.* **2018**, *136*, 51–60. [CrossRef]
23. Moustakas, L. A bibliometric analysis of research on social cohesion from 1994–2020. *Publications* **2022**, *10*, 5. [CrossRef]
24. De Cooman, B.C.; Estrin, Y.; Kim, S.K. Twinning-induced plasticity (TWIP) steels. *Acta Mater.* **2018**, *142*, 283–362. [CrossRef]
25. Bouaziz, O.; Allain, S.; Scott, C.P.; Cugy, P.; Barbier, D. High manganese austenitic twinning induced plasticity steels: A review of the microstructure properties relationships. *Curr. Opin. Solid State Mater. Sci.* **2011**, *15*, 141–168. [CrossRef]
26. Gutierrez-Urrutia, I.; Raabe, D. Dislocation and twin substructure evolution during strain hardening of an Fe–22 wt.% Mn–0.6 wt.% C TWIP steel observed by electron channeling contrast imaging. *Acta Mater.* **2011**, *59*, 6449–6462. [CrossRef]
27. Curtze, S.; Kuokkala, V.-T. Dependence of tensile deformation behavior of TWIP steels on stacking fault energy, temperature and strain rate. *Acta Mater.* **2010**, *58*, 5129–5141. [CrossRef]
28. Bouaziz, O.; Allain, S.; Scott, C.P. Effect of grain and twin boundaries on the hardening mechanisms of twinning-induced plasticity steels. *Scr. Mater.* **2008**, *58*, 484–487. [CrossRef]
29. Chen, S.; Rana, R.; Haldar, A.; Ray, R.K. Current state of Fe-Mn-Al-C low density steels. *Prog. Mater. Sci.* **2017**, *89*, 345–391. [CrossRef]
30. Gutierrez-Urrutia, I.; Zaefferer, S.; Raabe, D. The effect of grain size and grain orientation on deformation twinning in a Fe–22 wt.% Mn–0.6 wt.% C TWIP steel. *Mater. Sci. Eng. A* **2010**, *527*, 3552–3560. [CrossRef]
31. Steinmetz, D.R.; Jäpel, T.; Wietbrock, B.; Eisenlohr, P.; Gutierrez-Urrutia, I.; Saeed-Akbari, A.; Hickel, T.; Roters, F.; Raabe, D. Revealing the strain-hardening behavior of twinning-induced plasticity steels: Theory, simulations, experiments. *Acta Mater.* **2013**, *61*, 494–510. [CrossRef]
32. Pierce, D.T.; Jiménez, J.A.; Bentley, J.; Raabe, D.; Wittig, J.E. The influence of stacking fault energy on the microstructural and strain-hardening evolution of Fe–Mn–Al–Si steels during tensile deformation. *Acta Mater.* **2015**, *100*, 178–190. [CrossRef]
33. Kim, H.; Suh, D.-W.; Kim, N.J. Fe–Al–Mn–C lightweight structural alloys: A review on the microstructures and mechanical properties. *Sci. Technol. Adv. Mater.* **2013**, *14*, 014205. [CrossRef]
34. Allain, S.; Chateau, J.-P.; Bouaziz, O.; Migot, S.; Guelton, N. Correlations between the calculated stacking fault energy and the plasticity mechanisms in Fe–Mn–C alloys. *Mater. Sci. Eng. A* **2004**, *387*, 158–162. [CrossRef]
35. Curtze, S.; Kuokkala, V.-T.; Oikari, A.; Talonen, J.; Hänninen, H. Thermodynamic modeling of the stacking fault energy of austenitic steels. *Acta Mater.* **2011**, *59*, 1068–1076. [CrossRef]
36. Zambrano, O.A. Stacking fault energy maps of Fe–Mn–Al–C–Si steels: Effect of temperature, grain size, and variations in compositions. *J. Eng. Mater. Technol.* **2016**, *138*, 041010. [CrossRef]
37. Xiong, R.; Peng, H.; Si, H.; Zhang, W.; Wen, Y. Thermodynamic calculation of stacking fault energy of the Fe–Mn–Si–C high manganese steels. *Mater. Sci. Eng. A* **2014**, *598*, 376–386. [CrossRef]
38. Dumay, A.; Chateau, J.-P.; Allain, S.; Migot, S.; Bouaziz, O. Influence of addition elements on the stacking-fault energy and mechanical properties of an austenitic Fe–Mn–C steel. *Mater. Sci. Eng. A* **2008**, *483*, 184–187. [CrossRef]
39. Nakano, J.; Jacques, P.J. Effects of the thermodynamic parameters of the hcp phase on the stacking fault energy calculations in the Fe–Mn and Fe–Mn–C systems. *Calphad* **2010**, *34*, 167–175. [CrossRef]
40. Redlich, O.; Kister, A.T. Algebraic representation of thermodynamic properties and the classification of solutions. *Ind. Eng. Chem.* **1948**, *40*, 345–348. [CrossRef]
41. Tian, X.; Li, H.; Zhang, Y. Effect of Al content on stacking fault energy in austenitic Fe–Mn–Al–C alloys. *J. Mater. Sci.* **2008**, *43*, 6214–6222. [CrossRef]
42. Tian, X.; Zhang, Y. Effect of Si content on the stacking fault energy in γ-Fe–Mn–Si–C alloys: Part I. X-ray diffraction line profile analysis. *Mater. Sci. Eng. A* **2009**, *516*, 73–77. [CrossRef]
43. Pierce, D.T.; Jiménez, J.A.; Bentley, J.; Raabe, D.; Oskay, C.; Wittig, J.E. The influence of manganese content on the stacking fault and austenite/ε-martensite interfacial energies in Fe–Mn–(Al–Si) steels investigated by experiment and theory. *Acta Mater.* **2014**, *68*, 238–253. [CrossRef]
44. Saeed-Akbari, A.; Imlau, J.; Prahl, U.; Bleck, W. Derivation and variation in composition-dependent stacking fault energy maps based on subregular solution model in high-manganese steels. *Metall. Mater. Trans. A* **2009**, *40*, 3076–3090. [CrossRef]
45. Lee, S.-J.; Ushioda, K.; Fujii, H. Evaluation of stacking-fault energy in Fe-Mn based twinning-induced plasticity steels after friction stir welding. *Mater. Charact.* **2019**, *147*, 379–383. [CrossRef]

46. Kim, J.; De Cooman, B.C. On the stacking fault energy of Fe-18 Pct Mn-0.6 Pct C-1.5 Pct Al twinning-induced plasticity steel. *Metall. Mater. Trans. A* **2011**, *42*, 932–936. [CrossRef]
47. Kim, J.; Lee, S.-J.; De Cooman, B.C. Effect of Al on the stacking fault energy of Fe–18Mn–0.6C twinning-induced plasticity. *Scr. Mater.* **2011**, *65*, 363–366. [CrossRef]
48. Castañeda, J.A.; Zambrano, O.A.; Alcázar, G.A.; Rodríguez, S.A.; Coronado, J.J. Stacking fault energy determination in Fe-Mn-Al-C austenitic steels by X-ray diffraction. *Metals* **2021**, *11*, 1701. [CrossRef]
49. Peng, X.; Zhu, D.-Y.; Hu, Z.-M.; Wang, M.-J.; Liu, L.-L.; Liu, H.-J. Effect of carbon content on stacking fault energy of Fe-20Mn-3Cu TWIP steel. *J. Iron Steel Res. Int.* **2014**, *21*, 116–120. [CrossRef]
50. Wang, C.; Cai, W.; Sun, C.; Li, X.; Qian, L.; Jiang, J. Strain rate effects on mechanical behavior and microstructure evolution with the sequential strains of TWIP steel. *Mater. Sci. Eng. A* **2022**, *835*, 142673. [CrossRef]
51. Hokka, M.; Curtze, S.; Kuokkala, V.-T.; Peura, P.; Oyj, R. Dynamic response of high-manganese TWIP steels. In Proceedings of the 2008 SEM XI International Congress and Exposition on Experimental and Applied Mechanics, Orlando, FL, USA, 2–5 June 2008.
52. Xu, S.; Ruan, D.; Beynon, J.H.; Rong, Y. Dynamic tensile behaviour of TWIP steel under intermediate strain rate loading. *Mater. Sci. Eng. A* **2013**, *573*, 132–140. [CrossRef]
53. Kang, M.; Park, J.; Sohn, S.S.; Kim, H.S.; Kim, N.J.; Lee, S. Interpretation of quasi-static and dynamic tensile behavior by digital image correlation technique in TWinning Induced Plasticity (TWIP) and low-carbon steel sheets. *Mater. Sci. Eng. A* **2017**, *693*, 170–177. [CrossRef]
54. Allain, S.; Chateau, J.-P.; Bouaziz, O. A physical model of the twinning-induced plasticity effect in a high manganese austenitic steel. *Mater. Sci. Eng. A* **2004**, *387*, 143–147. [CrossRef]
55. Boja, M.S.; Giordana, M.F.; Malarria, J.; Druker, A.V. Procedures for microstructurally conditioning an Fe-22Mn-0.6C-1.5Al TWIP steel for optimal mechanical behaviour. *Mater. Charact.* **2023**, *199*, 112790. [CrossRef]
56. Bracke, L.; Kestens, L.; Penning, J. Direct observation of the twinning mechanism in an austenitic Fe–Mn–C steel. *Scr. Mater.* **2009**, *61*, 220–222. [CrossRef]
57. Idrissi, H.; Renard, K.; Ryelandt, L.; Schryvers, D.; Jacques, P.J. On the mechanism of twin formation in Fe–Mn–C TWIP steels. *Acta Mater.* **2010**, *58*, 2464–2476. [CrossRef]
58. Kim, J.-K. In-situ TEM investigation of deformation mechanisms of twinning-induced plasticity steel. *Mater. Charact.* **2023**, *196*, 112583. [CrossRef]
59. Jin, J.-E.; Lee, Y.-K. Strain hardening behavior of a Fe–18Mn–0.6C–1.5Al TWIP steel. *Mater. Sci. Eng. A* **2009**, *527*, 157–161. [CrossRef]
60. Wang, S.-H.; Liu, Z.-Y.; Wang, G.-D.; Liu, J.-L.; Liang, G.-F.; Li, Q.-L. Effects of twin-dislocation and twin-twin interactions on the strain hardening behavior of TWIP steels. *J. Iron Steel Res. Int.* **2010**, *17*, 70–74. [CrossRef]
61. Idrissi, H.; Renard, K.; Schryvers, D.; Jacques, P.J. On the relationship between the twin internal structure and the work-hardening rate of TWIP steels. *Scr. Mater.* **2010**, *63*, 961–964. [CrossRef]
62. Vercammen, S.; Blanpain, B.; De Cooman, B.C.; Wollants, P. Cold rolling behaviour of an austenitic Fe–30Mn–3Al–3Si TWIP-steel: The importance of deformation twinning. *Acta Mater.* **2004**, *52*, 2005–2012. [CrossRef]
63. Lee, S.-J.; Kim, J.; Kane, S.N.; De Cooman, B.C. On the origin of dynamic strain aging in twinning-induced plasticity steels. *Acta Mater.* **2011**, *59*, 6809–6819. [CrossRef]
64. Liang, Z.Y.; Luo, Z.C.; Huang, M.X. Temperature dependence of strengthening mechanisms in a twinning-induced plasticity steel. *Int. J. Plast.* **2019**, *116*, 192–202. [CrossRef]
65. Torganchuk, V.; Belyakov, A.; Kaibyshev, R. Improving mechanical properties of 18% Mn TWIP steels by cold rolling and annealing. *Metals* **2019**, *9*, 776. [CrossRef]
66. Pereira, A.B.; Fernandes, F.A.; Filipe, B. Effect of deformation path on the microstructure and mechanical behavior of TWIP980 steel. *J. Manuf. Mater. Process.* **2019**, *3*, 12. [CrossRef]
67. Tewary, N.K.; Ghosh, S.K.; Chatterjee, S. Deformation behaviour of low carbon high Mn twinning-induced plasticity steel. *Proc. Inst. Mech. Eng. Part C J. Mech. Eng. Sci.* **2019**, *233*, 763–771. [CrossRef]
68. Tewary, N.K.; Ghosh, S.K.; Chatterjee, S.; Ghosh, A. Deformation and annealing behaviour of dual phase TWIP steel from the perspective of residual stress, faults, microstructures and mechanical properties. *Mater. Sci. Eng. A* **2018**, *733*, 43–58. [CrossRef]
69. Xue, H.; Yuan, H.; Guo, K.; Zhang, Z.; Zhang, M. Microstructure evolution and recrystallization temperature change of cold-rolled Fe–19Mn–0.6C twinning-induced plasticity steel during annealing. *Metals* **2021**, *11*, 1181. [CrossRef]
70. Kalinenko, A.; Kusakin, P.; Belyakov, A.; Kaibyshev, R.; Molodov, D.A. Microstructure and mechanical properties of a high-Mn TWIP steel subjected to cold rolling and annealing. *Metals* **2017**, *7*, 571. [CrossRef]
71. Tewary, N.K.; Ghosh, S.K.; Chatterjee, S. Effect of annealing on microstructure and mechanical behaviour of cold rolled low C, high Mn TWIP steel. *Int. J. Metall. Eng.* **2015**, *4*, 12–23.
72. Tian, Y.Z.; Bai, Y.; Chen, M.C.; Shibata, A.; Terada, D.; Tsuji, N. Enhanced strength and ductility in an ultrafine-grained Fe-22Mn-0.6C austenitic steel having fully recrystallized structure. *Metall. Mater. Trans. A* **2014**, *45*, 5300–5304. [CrossRef]

73. Dini, G.; Najafizadeh, A.; Ueji, R.; Monir-Vaghefi, S.M. Improved tensile properties of partially recrystallized submicron grained TWIP steel. *Mater. Lett.* **2010**, *64*, 15–18. [CrossRef]
74. Dini, G.; Najafizadeh, A.; Ueji, R.; Monir-Vaghefi, S.M. Tensile deformation behavior of high manganese austenitic steel: The role of grain size. *Mater. Des.* **2010**, *31*, 3395–3402. [CrossRef]
75. Yuan, X.; Chen, L.; Zhao, Y.; Di, H.; Zhu, F. Dependence of grain size on mechanical properties and microstructures of high manganese austenitic steel. *Procedia Eng.* **2014**, *81*, 143–148. [CrossRef]
76. Lan, P.; Zhang, J. Tensile property and microstructure of Fe-22Mn-0.5C TWIP steel. *Mater. Sci. Eng. A* **2017**, *707*, 373–382. [CrossRef]
77. Tewary, N.K.; Ghosh, S.K.; Mandal, A.; Chakrabarti, D.; Chatterjee, S. Effect of annealing on the microstructure, texture and mechanical properties of a dual-phase ultrahigh-strength TWIP steel. *Metall. Mater. Trans. A* **2020**, *51*, 4483–4498. [CrossRef]
78. Kang, S.; Jung, Y.-S.; Jun, J.-H.; Lee, Y.-K. Effects of recrystallization annealing temperature on carbide precipitation, microstructure, and mechanical properties in Fe–18Mn–0.6C–1.5Al TWIP steel. *Mater. Sci. Eng. A* **2010**, *527*, 745–751. [CrossRef]
79. Başkurt, Ş.; Hayat, F.; Sezgin, C.T.; Şahin, S. Influences of heat treatment parameters on microstructure and mechanical behavior of TWIP steel. *Manuf. Technol. Appl.* **2024**, *5*, 203–213. [CrossRef]
80. Schinhammer, M.; Pecnik, C.M.; Rechberger, F.; Hänzi, A.C.; Löffler, J.F.; Uggowitzer, P.J. Recrystallization behavior, microstructure evolution and mechanical properties of biodegradable Fe–Mn–C(–Pd) TWIP alloys. *Acta Mater.* **2012**, *60*, 2746–2756. [CrossRef]
81. Tewary, N.K.; Ghosh, S.K.; Saha, R.; Chatterjee, S. Deformation and annealing behaviour of a low carbon high Mn TWIP steel microalloyed with Ti. *Philos. Mag.* **2019**, *99*, 2487–2516. [CrossRef]
82. Zhang, J.; Bai, Y.; Fan, W.; Zhang, G.; Zhang, W.; Yang, Y.; Hao, H. Microstructure and mechanical properties of a new TWIP steel under different heat treatments. *Materials* **2024**, *17*, 2080. [CrossRef]
83. Fabrègue, D.; Bouaziz, O.; Barbier, D. Nano-twinned steel exhibits high mechanical properties obtained through ultra-rapid heat treatment. *Mater. Sci. Eng. A* **2018**, *712*, 765–771. [CrossRef]
84. Tewary, N.K.; Ghosh, S.K.; Chatterjee, S. Effect of Al content in low carbon high manganese TWIP steel. *Key Eng. Mater.* **2016**, *706*, 16–22. [CrossRef]
85. Song, S.W.; Lee, T.; Lee, C.S. Graded grain structure to improve hydrogen-embrittlement resistance of TWIP steel. *Crystals* **2020**, *10*, 1045. [CrossRef]
86. Koyama, M.; Akiyama, E.; Tsuzaki, K. Hydrogen embrittlement in a Fe–Mn–C ternary twinning-induced plasticity steel. *Corros. Sci.* **2012**, *54*, 1–4. [CrossRef]
87. Koyama, M.; Akiyama, E.; Tsuzaki, K. Effect of hydrogen content on the embrittlement in a Fe–Mn–C twinning-induced plasticity steel. *Corros. Sci.* **2012**, *59*, 277–281. [CrossRef]
88. Koyama, M.; Akiyama, E.; Sawaguchi, T.; Raabe, D.; Tsuzaki, K. Hydrogen-induced cracking at grain and twin boundaries in an Fe–Mn–C austenitic steel. *Scr. Mater.* **2012**, *66*, 459–462. [CrossRef]
89. Koyama, M.; Akiyama, E.; Tsuzaki, K.; Raabe, D. Hydrogen-assisted failure in a twinning-induced plasticity steel studied under in situ hydrogen charging by electron channeling contrast imaging. *Acta Mater.* **2013**, *61*, 4607–4618. [CrossRef]
90. Khanchandani, H.; Rolli, R.; Schneider, H.-C.; Kirchlechner, C.; Gault, B. Hydrogen embrittlement of twinning-induced plasticity steels: Contribution of segregation to twin boundaries. *Scr. Mater.* **2023**, *225*, 115187. [CrossRef]
91. Wang, D.; Lu, X.; Deng, Y.; Guo, X.; Barnoush, A. Effect of hydrogen on nanomechanical properties in Fe-22Mn-0.6C TWIP steel revealed by in-situ electrochemical nanoindentation. *Acta Mater.* **2019**, *166*, 618–629. [CrossRef]
92. Park, I.-J.; Lee, S.-M.; Jeon, H.-H.; Lee, Y.-K. The advantage of grain refinement in the hydrogen embrittlement of Fe–18Mn–0.6C twinning-induced plasticity steel. *Corros. Sci.* **2015**, *93*, 63–69. [CrossRef]
93. Chun, Y.S.; Park, K.-T.; Lee, C.S. Delayed static failure of twinning-induced plasticity steels. *Scr. Mater.* **2012**, *66*, 960–965. [CrossRef]
94. Dieudonné, T.; Marchetti, L.; Wery, M.; Chêne, J.; Allely, C.; Cugy, P.; Scott, C.P. Role of copper and aluminum additions on the hydrogen embrittlement susceptibility of austenitic Fe–Mn–C TWIP steels. *Corros. Sci.* **2014**, *82*, 218–226. [CrossRef]
95. Dong, F.; Venezuela, J.; Li, H.; Shi, Z.; Zhou, Q.; Chen, L.; Chen, J.; Du, L.; Atrens, A. Enhancement of hydrogen embrittlement resistance in a Fe-18Mn-0.6C twinning induced plasticity steel by copper alloying. *Acta Mater.* **2023**, *254*, 118888. [CrossRef]
96. Lee, S.-M.; Park, I.-J.; Jung, J.-G.; Lee, Y.-K. The effect of Si on hydrogen embrittlement of Fe-18Mn-0.6C-xSi twinning-induced plasticity steels. *Acta Mater.* **2016**, *103*, 264–272. [CrossRef]
97. Chen, L.; Antonov, S.; Song, K.; Zhi, H.; Li, W.; Chen, Y.; Hu, K.; Zhong, Y.; Su, Y.; Qiao, L. Effect of solute atoms (C, Al and Si) on hydrogen embrittlement resistance of high-Mn TWIP steels. *Corros. Sci.* **2022**, *203*, 110376. [CrossRef]
98. Hamada, A.S.; Karjalainen, L.P.; Puustinen, J. Fatigue behavior of high-Mn TWIP steels. *Mater. Sci. Eng. A* **2009**, *517*, 68–77. [CrossRef]
99. Shao, C.W.; Zhang, P.; Wang, X.G.; Wang, Q.; Zhang, Z.F. High-cycle fatigue behavior of TWIP steel with graded grains: Breaking the rule of mixture. *Mater. Res. Lett.* **2019**, *7*, 26–32. [CrossRef]

100. Klein, M.W.; Blinn, B.; Smaga, M.; Beck, T. High cycle fatigue behavior of high-Mn TWIP steel with different surface morphologies. *Int. J. Fatigue* **2020**, *134*, 105499. [CrossRef]
101. Wang, Q.; Zhao, Y.; Fan, Y.; Zhao, P.; Fan, P. Effect of pre-strain on high cycle fatigue property of TWIP steel. *Mater. Sci. Technol.* **2023**, *39*, 2117–2123. [CrossRef]
102. Guo, P.; Qian, L.; Meng, J.; Liu, S.; Zhang, F. Effect of Al on the low cycle fatigue deformation behavior and microstructure evolution of Fe–22Mn–0.6C TWIP steel. *J. Mater. Res. Technol.* **2024**, *30*, 2086–2098. [CrossRef]
103. Song, D.; Vormwald, M.; Beier, H.T. Low-cycle fatigue behavior and life-prediction model of high-manganese twinning-induced plasticity steels with different loading orientations, pre-strains, and ambient temperatures. *Int. J. Fatigue* **2025**, *200*, 109123. [CrossRef]
104. Junak, G.; Jabłońska, M.B. The studies of low-cycle fatigue behavior of high manganese TWIP steel. *Adv. Sci. Technol. Res. J.* **2025**, *19*, 237–253. [CrossRef]
105. Luo, Z.C.; Huang, M.X. Revealing the fracture mechanism of twinning-induced plasticity steels. *Steel Res. Int.* **2018**, *89*, 1700433. [CrossRef]
106. Cai, W.; Wang, C.; Sun, C.; Qian, L.; Fu, M.W. Microstructure evolution and fracture behaviour of TWIP steel under dynamic loading. *Mater. Sci. Eng. A* **2022**, *851*, 143657. [CrossRef]
107. Hwang, J.-K. Fracture behavior of twinning-induced plasticity steel during wire drawing. *J. Mater. Res. Technol.* **2020**, *9*, 4527–4537. [CrossRef]
108. De Barbieri, F.; Donoso, J.; Landes, J.; Monsalve, A.; Perez Ipiña, J.; Jorge-Badiola, D.; Inostroza, E. J integral fracture toughness of a twinning-induced plasticity steel Fe–Mn–C–Cr: Effect of Cr content. *J. Mater. Res. Technol.* **2026**, *42*, 10036–10051. [CrossRef]
109. Dey, D.; Pal, A.; Biyani, P.; Mandal, P.; Pal, S.; Das, S.; Dey, S.; Ghosh, M. Developing new high-entropy alloys with enhanced hardness using a hybrid machine learning approach: Integrating interpretability and NSGA-II optimization. *J. Mater. Sci.* **2025**, *60*, 4820–4845. [CrossRef]
110. Sinha, S.; Das, P.; Mallick, A.B.; Ghosh, M. Machine learning-based regression modelling for yield strength prediction in TWIP steel. In *International Conference on Data Management, Analytics & Innovation*; Springer: Berlin/Heidelberg, Germany, 2025; pp. 369–379.
111. Zhou, X.; Xu, J.; Meng, L.; Wang, W.; Zhang, N.; Jiang, L. Machine-learning-assisted composition design for high-yield-strength TWIP steel. *Metals* **2024**, *14*, 952. [CrossRef]
112. Tanaka, M.; Sasaki, K.; Punyafu, J.; Muramatsu, M.; Murayama, M. Machine-learning-aided analysis of relationship between crystal defects and macroscopic mechanical properties of TWIP steel. *Sci. Rep.* **2025**, *15*, 14435. [CrossRef]
113. Wu, R.; Zhang, Y.; Peng, Z.; Song, D.; Li, H. Predicting multiple fatigue properties of twinning-induced plasticity steels by black-box and white-box machine learning. *Mech. Mater.* **2025**, *205*, 105307. [CrossRef]
114. Song, D.; Pei, J.; Xiao, Y.; Wu, R.; Li, H. Predicting the whole-life stress amplitude evolution of high-Mn TWIP steel under complex loading conditions using fatigue failure criteria and machine learning. *Int. J. Fatigue* **2025**, *206*, 109449. [CrossRef]
115. Li, Z.; Dai, Y. Research progress on properties of TWIP steel for automobile. *Trans. Mater. Heat Treat.* **2019**, *40*, 1–7.
116. Yang, J.; Zhu, M. Evolution of compositions and properties of CaO–SiO_2 based mold flux for continuous casting high Mn steel. *ISIJ Int.* **2016**, *56*, 2191–2198. [CrossRef]
117. Kwok, T.W.J.; Dye, D. A review of the processing, microstructure and property relationships in medium Mn steels. *Int. Mater. Rev.* **2023**, *68*, 1098–1134. [CrossRef]
118. Lee, H.; Jo, M.C.; Sohn, S.S.; Kim, S.-H.; Song, T.; Kim, S.-K.; Kim, H.S.; Kim, N.J.; Lee, S. Microstructural evolution of liquid metal embrittlement in resistance-spot-welded galvanized twinning-induced plasticity (TWIP) steel sheets. *Mater. Charact.* **2019**, *147*, 233–241. [CrossRef]

Disclaimer/Publisher's Note: The statements, opinions and data contained in all publications are solely those of the individual author(s) and contributor(s) and not of MDPI and/or the editor(s). MDPI and/or the editor(s) disclaim responsibility for any injury to people or property resulting from any ideas, methods, instructions or products referred to in the content.